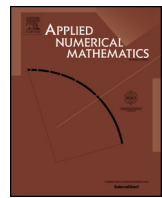




Contents lists available at ScienceDirect

Applied Numerical Mathematics

[www.elsevier.com/locate/apnum](http://www.elsevier.com/locate/apnum)



# Projected finite elements for reaction–diffusion systems on stationary closed surfaces



N. Tuncer<sup>a</sup>, A. Madzvamuse<sup>b,\*</sup>, A.J. Meir<sup>c</sup>

<sup>a</sup> Department of Mathematical Sciences, Florida Atlantic University, United States

<sup>b</sup> School of Mathematical and Physical Sciences, Department of Mathematics, University of Sussex, Brighton, BN1 9QH, United Kingdom

<sup>c</sup> Department of Mathematics and Statistics, Auburn University, United States

## ARTICLE INFO

### Article history:

Received 1 July 2013

Received in revised form 24 August 2014

Accepted 9 December 2014

Available online 29 April 2015

### Keywords:

Radially projected finite elements

Reaction–diffusion systems

Pattern formation

Surface geometry

Surface partial differential equations

## ABSTRACT

In this paper we present a robust, efficient and accurate finite element method for solving reaction–diffusion systems on stationary spheroidal surfaces (these are surfaces which are deformations of the sphere such as ellipsoids, dumbbells, and heart-shaped surfaces) with potential applications in the areas of developmental biology, cancer research, wound healing, tissue regeneration, and cell motility among many others where such models are routinely used. Our method is inspired by the radially projected finite element method introduced in [39]. (Hence the name “projected” finite element method.) The advantages of the projected finite element method are that it is easy to implement and that it provides a conforming finite element discretization which is “logically” rectangular. To demonstrate the robustness, applicability and generality of this numerical method, we present solutions of reaction–diffusion systems on various spheroidal surfaces. We show that the method presented in this paper preserves positivity of the solutions of reaction–diffusion equations which is not generally true for Galerkin type methods. We conclude that surface geometry plays a pivotal role in pattern formation. For a fixed set of model parameter values, different surfaces give rise to different pattern generation sequences of either spots or stripes or a combination (observed as circular spot-stripe patterns). These results clearly demonstrate the need for detailed theoretical analytical studies to elucidate how surface geometry and curvature influence pattern formation on complex surfaces.

© 2015 The Authors. Published by Elsevier B.V. on behalf of IMACS. This is an open access article under the CC BY license (<http://creativecommons.org/licenses/by/4.0/>).

## 1. Introduction

For many centuries, the problem of pattern formation has fascinated experimentalists and theoreticians alike. Despite this long standing interest, understanding how patterns form on real biological surfaces and how surface geometry and curvature influence patterning remains largely an uncharted research area with numerous unanswered questions [41,53]. Several studies have shown that reaction–diffusion equations (RDEs) can be used for describing gross patterning behavior in developmental biology [41]. The majority of studies for pattern formation by RDEs to date have simply studied RDEs on planar domains [34,36,37,41,45]. Although this is perfectly justifiable in some biological species such as butterfly patterns [47], and stingrays [2], it is not for many species such as snakes, eel, fish, and leopards [41] where surface geometry and curvature play a crucial role in the emergence and orientation of patterns on biologically realistic surfaces. Other examples

\* Corresponding author.

E-mail addresses: [necibe-tuncer@utulsa.edu](mailto:necibe-tuncer@utulsa.edu) (N. Tuncer), [a.madzvamuse@sussex.ac.uk](mailto:a.madzvamuse@sussex.ac.uk) (A. Madzvamuse), [ajm@auburn.edu](mailto:ajm@auburn.edu) (A.J. Meir).

where surface geometry and curvature play a key role in pattern formation are sea shells [38], zebra stripes [40,41], lady beetles [30], repeated structures in skin organ formation [49], zebra fish [43] and pomacanthus fish [26].

In the area of numerical analysis, there are various methods for approximating solutions of partial differential equations posed on surfaces. Examples include (but not limited to) the method of lines [7], surface finite element methods on triangulated surfaces [1,15,16,18,19], implicit finite element methods using level set descriptions of the surfaces [17,18,42,48], diffuse interface methods of which phase-fields are an example [5,10,20], particle methods using level set descriptions of the surface [13,23,25,29] and closest-point methods [32,33]. In all these methods the continuous surface is approximated by a discrete surface thereby introducing a *geometrical error*. In most of these studies (except for the closest point method), the numerical methods are designed to treat models on moving surfaces or interfaces or moving manifolds. In this article, we are dealing with stationary surfaces and evolving surfaces are the subject of our current studies. A key issue is how the surface description is encoded into the numerical method. For the surface finite elements, the surface is approximated by a triangulated surface. The geometrical description of the surface is encoded through the knowledge of the vertices of the triangulation. A geometrical error is introduced in carrying out the surface triangulation. On the other hand, numerical methods based on implicit surfaces require the knowledge of the level set function that defines the surface geometry [19]. A key difference between these methods and the projected finite element method (PFEM) is that the latter does not suffer from the geometric error since the surface is not approximated but described exactly, however, this is at the expense of requiring a map that generates the surface.

The PFEM proposed in this article is inspired by the radially projected finite element method which was used to compute approximate numerical solutions for partial differential equations on stationary spheroidal surfaces such as spheres, ellipsoids, and tori [39,52]. The PFEM gives a geometrically exact discretization of spheroidal surfaces (the geometry is not approximated, but represented exactly). This is attractive for numerical simulations since the resulting finite element discretization is conforming and is “logically rectangular.” The PFEM is easy to implement and incorporate into existing finite element codes.

Our article is structured as follows. Reaction–diffusion systems defined on arbitrary spheroidal surfaces are formulated in Section 2. Within this framework we state preliminaries and introduce the notation for surface gradients to be used throughout the paper. We present the PFEM in Section 3 and demonstrate how the method is used to generate the surface mesh triangulation describing the continuous surface. Furthermore, we develop and analyze the PFEM used to approximate solutions of RDEs on various spheroidal surfaces. Section 4 is devoted to numerical simulations where we validate our theoretical error analysis as well as demonstrate the diversity of patterns obtained on surfaces. Finally, in Section 5 we conclude and discuss our findings and lay down foundations for future research.

## 2. Model equations on stationary spheroidal surfaces

Let  $\mathcal{S}$  be a closed, compact, smooth, hypersurface in  $\mathbb{R}^{N+1}$ . Let  $\mathbf{n}$  denote the unit outer normal to  $\mathcal{S}$ , and let  $U$  be any open subset of  $\mathbb{R}^{N+1}$  containing  $\mathcal{S}$ , then for any function  $u$  which is differentiable in  $U$ , we define the tangential gradient on  $\mathcal{S}$  by,

$$\nabla_{\mathcal{S}} u = \nabla u - (\nabla u \cdot \mathbf{n}) \mathbf{n},$$

where  $\cdot$  denotes the dot product and  $\nabla$  denotes the gradient in  $\mathbb{R}^{N+1}$ . The tangential gradient is the projection of the gradient onto the tangent plane, thus  $\nabla_{\mathcal{S}} u \cdot \mathbf{n} = 0$ . The Laplace–Beltrami operator on the surface  $\mathcal{S}$  is defined to be the tangential divergence of the tangential gradient  $\Delta_{\mathcal{S}} u = \nabla_{\mathcal{S}} \cdot \nabla_{\mathcal{S}} u$ . For a vector function  $\mathbf{u} = (u_1, u_2, \dots, u_{N+1}) \in \mathbb{R}^{N+1}$  the tangential divergence is defined by

$$\nabla_{\mathcal{S}} \cdot \mathbf{u} = \nabla \cdot \mathbf{u} - \sum_{i=1}^{N+1} (\nabla u_i \cdot \mathbf{n}) n_i.$$

For notational simplicity, let us denote the partial time-derivative of  $u$  by

$$\partial_t u := u_t = \frac{\partial u}{\partial t}.$$

In this study, we restrict  $\mathbf{u} = (u, v)^T$  to be a vector of only two chemical species resident on the surface  $\mathcal{S}$ . Extensions to multi-species will be conducted in future studies. The evolution equations for reaction–diffusion on stationary surfaces can be readily obtained from the law of mass conservation and these, in non-dimensional form, are of the form [37,41]

$$\begin{cases} \partial_t u - \Delta_{\mathcal{S}} u = \gamma f(u, v), \\ \partial_t v - d \Delta_{\mathcal{S}} v = \gamma g(u, v), \end{cases} \quad (1)$$

where  $u$  and  $v$  only interact through the nonlinear reaction terms  $f(u, v)$  and  $g(u, v)$  in the absence of cross-diffusion. In (1),  $d > 1$  is the non-dimensionalized diffusion coefficient and  $\gamma$  is a positive scaling parameter [41]. Since we are dealing with stationary surfaces, the nonlinear reaction kinetics,  $f(u, v)$  and  $g(u, v)$  can be, either a pure, or cross activator-inhibitor

mechanism where  $u$  and  $v$  represent the activator and inhibitor respectively [11,40]. For illustrative purposes we consider the *activator-depleted* substrate model [22,44,46] also known as the Brusselator model whose reaction kinetics are given by

$$f(u, v) = a - u + u^2v \quad \text{and} \quad g(u, v) = b - u^2v,$$

where  $a$  and  $b$  are positive parameters. Other plausible reactions such as the Gierer–Meinhardt [22], Thomas [50], or BVPM [2] kinetics can be easily incorporated into our framework.

### 3. Projected finite element method for reaction–diffusion systems

#### 3.1. Preliminaries

In order to derive a weak formulation of the system (1), we first define the function spaces in which we seek solutions of the system. For the reader's convenience we give brief definitions of the Sobolev spaces and their norms occurring in this paper. We use the standard notation for Lebesgue and Sobolev spaces defined on the surface  $\mathcal{S}$  (see [24] for further details). In particular for  $\alpha = (\alpha_1, \alpha_2, \alpha_3) \in \mathbb{N}^3$ , a multi-index with  $|\alpha| = \alpha_1 + \alpha_2 + \alpha_3$ , the Lebesgue and Sobolev spaces are defined, respectively, as

$$L^p(\mathcal{S}) = \left\{ u : \int_{\mathcal{S}} |u|^p < \infty \right\}$$

and

$$W^{m,p}(\mathcal{S}) = \left\{ u \in L^p(\mathcal{S}) : \int_{\mathcal{S}} |\partial_{\mathcal{S}}^{\alpha} u|^p < \infty, \text{ for } |\alpha| \leq m \right\},$$

where  $\partial_{\mathcal{S}}^{\alpha}$  is the tangential  $\alpha$  partial derivative. Note that unlike the regular derivatives, higher order tangential derivatives do not commute. We use the convention that  $W^{0,p}(\mathcal{S})$  is  $L^p(\mathcal{S})$ . Recall that  $W^{m,p}(\mathcal{S})$  is a Banach space equipped with the norm

$$\|u\|_{W^{m,p}(\mathcal{S})} = \left( \sum_{|\alpha| \leq m} \|\partial_{\mathcal{S}}^{\alpha} u\|_{L^p(\mathcal{S})}^p \right)^{\frac{1}{p}}, \quad 1 \leq p < \infty.$$

We also use the common convention that  $H^m(\mathcal{S}) = W^{m,2}(\mathcal{S})$ , and make use of the  $H^m(\mathcal{S})$  semi-norm defined by

$$|u|_{H^m(\mathcal{S})} = \left( \sum_{|\alpha|=m} \|\partial_{\mathcal{S}}^{\alpha} u\|_{L^2(\mathcal{S})}^2 \right)^{\frac{1}{2}}.$$

We denote  $\mathcal{H} = H^1(\mathcal{S}) \times H^1(\mathcal{S})$ , the space of vector valued functions  $(u, v)$  such that  $u \in H^1(\mathcal{S})$  and  $v \in H^1(\mathcal{S})$ . This space is equipped with the graph norm

$$\|(u, v)\|_{\mathcal{H}} = \sqrt{\|u\|_{H^1(\mathcal{S})}^2 + \|v\|_{H^1(\mathcal{S})}^2}.$$

The dual of  $\mathcal{H}$  is denoted by  $\mathcal{H}^*$ . Clearly a solution  $(u, v)$  of (1) is a vector of functions of the spatial variable  $\mathbf{x}$  and the time variable  $t$ . We denote  $L^2(0, T; \mathcal{H})$  the space which consists of  $\mathcal{H}$ -valued functions  $(u, v) : [0, T] \rightarrow \mathcal{H}$ . In other words we consider  $(u, v)$  as a mapping of  $t$  into the space of  $\mathcal{H}$ -valued functions of  $\mathbf{x}$ . The space  $L^2(0, T; \mathcal{H})$  is equipped with the norm

$$\|(u, v)\|_{L^2(0, T; \mathcal{H})} = \left( \int_0^T \|(u, v)\|_{\mathcal{H}}^2 dt \right)^{1/2}.$$

We denote the inner product in  $L^2(\mathcal{S})$  by

$$(u, v) = \int_{\mathcal{S}} uv, \quad \text{for } u, v \in L^2(\mathcal{S}). \tag{2}$$

Let  $\mathbf{x} = (x_1, x_2, \dots, x_{N+1})$  be a vector in  $\mathbb{R}^{N+1}$ , then the Euclidean and maximum norms are

$$\|\mathbf{x}\|_2 = \sqrt{x_1^2 + x_2^2 + \dots + x_{N+1}^2} \text{ and } \|\mathbf{x}\|_{\infty} = \max \{|x_1|, |x_2|, \dots, |x_{N+1}| \}$$

respectively.

### 3.2. Weak formulation of the reaction-diffusion system

We now derive a weak formulation of (1). Let  $\omega, v \in H^1(\mathcal{S})$  be test functions. Multiplying (1) by  $\omega$  and  $v$  and integrating over the surface  $\mathcal{S}$ , we get the following weak formulation: Find  $(u, v) \in L^2(0, T; \mathcal{H})$  with  $(\partial_t u, \partial_t v) \in L^2(0, T; \mathcal{H}^*)$  such that

$$\begin{cases} (\partial_t u, \omega) + (\nabla_{\mathcal{S}} u, \nabla_{\mathcal{S}} \omega) + \gamma(u, \omega) = \gamma(a + u^2 v, \omega), \\ (\partial_t v, v) + d(\nabla_{\mathcal{S}} u, \nabla_{\mathcal{S}} v) = \gamma(b - u^2 v, v), \end{cases} \quad (3)$$

for all  $(\omega, v) \in \mathcal{H}$  a.e.  $t > 0$ . In the above, we have exploited the fact that we are working on a closed surface (with no boundary). In the case that this is open (the surface has a boundary), homogeneous Neumann boundary conditions (zero-flux) are prescribed and identical equations are obtained.

To approximate solutions of (3) we apply the Galerkin finite element method (which consists of defining a similar problem on a finite dimensional subspace). Our problem now consists of constructing a finite dimensional subspace  $X$  of  $\mathcal{H}$ . We construct the space  $X$  using projection operators.

#### 3.2.1. Projection operators and surface mesh generation

The radial projection introduced in [39] is used not only to generate a quality mesh on the sphere, but also to define a conforming finite element method with optimal convergence rates. In this paper, we introduce projection operators to generate the mesh on closed surfaces which are the deformation of the sphere such as (but not limited to) ellipsoids, cylinders, dumbbells and heart-shaped surfaces. In Section 3.3, we show that the finite element spaces constructed by projection operators yield methods which have optimal convergence rates.

First, let us define the radial projection [39].

**Definition 1.** Let  $B$  denote a surface of a cube with side length  $2l$ , and let  $\mathcal{S}_r$  be a sphere with radius  $r$ . We denote the radial projection from  $B$  onto  $\mathcal{S}_r$  by  $P_{\mathcal{R}}$ . It is defined by

$$P_{\mathcal{R}}(\mathbf{x}) = \frac{r\|\mathbf{x}\|_{\infty}}{l\|\mathbf{x}\|_2} \mathbf{x}. \quad (4)$$

**Remark 1.** The radial projection  $P_{\mathcal{R}}$  and its inverse  $P_{\mathcal{R}}^{-1}$  are Lipschitz continuous [39,52].

The following example shows how the radial projection can be modified to generate a mesh on a cylindrical surface. Consider a cylinder with spherical caps given by

$$1 = \begin{cases} x^2 + y^2 + (z - 1)^2 & \text{if } 1 < z \leq 2, \\ x^2 + y^2 & \text{if } -1 \leq z \leq 1, \\ x^2 + y^2 + (z + 1)^2 & \text{if } -2 < z \leq -1. \end{cases}$$

Let  $B$  be the rectangular box with bottom face at  $z = -2$  and top face at  $z = 2$  and whose top and bottom faces are given by the square  $[-1, 1] \times [-1, 1]$  (see Fig. 1). The radial projection from  $B$  onto the cylinder with spherical caps is:

$$P_{\mathcal{R}}(\mathbf{x}) = \begin{cases} \frac{r\|\mathbf{x} - \hat{\mathbf{x}}\|_{\infty}}{b\|\mathbf{x} - \hat{\mathbf{x}}\|_2} \mathbf{x} + \hat{\mathbf{x}} & \text{if } 1 < z \leq 2, \\ (\frac{r\|\mathbf{x}\|_{\infty}}{b\|\mathbf{x}\|_2} x_1, \frac{r\|\mathbf{x}\|_{\infty}}{b\|\mathbf{x}\|_2} x_2, x_3), & \text{if } -1 \leq z \leq 1, \\ \frac{r\|\mathbf{x} + \hat{\mathbf{x}}\|_{\infty}}{b\|\mathbf{x} + \hat{\mathbf{x}}\|_2} \mathbf{x} - \hat{\mathbf{x}} & \text{if } -2 < z \leq -1. \end{cases} \quad (5)$$

where  $\hat{\mathbf{x}} = (0, 0, 1)$  and  $r = 1$  and  $b = 1$ . A mesh on the rectangular box and mesh generated by the radial projection  $P_{\mathcal{R}}(\mathbf{x})$  on the cylinder with spherical caps are shown in Fig. 1.

Next, we define the projection operators which we use to introduce the projected finite element method.

**Definition 2 (Projection operator).** Let  $\mathcal{T}$  be a Lipschitz continuous mapping from sphere with radius  $r$ ,  $\mathcal{S}_r$ , to the surface  $\mathcal{S}$ , whose inverse  $\mathcal{T}^{-1} : \mathcal{S} \rightarrow \mathcal{S}_r$  is also Lipschitz continuous. Namely, there exist constants  $c$  and  $C$  such that

$$\|\mathcal{T}(\mathbf{x}_1) - \mathcal{T}(\mathbf{x}_2)\| \leq c\|\mathbf{x}_1 - \mathbf{x}_2\|, \quad \text{and} \quad \|\mathcal{T}^{-1}(\mathbf{y}_1) - \mathcal{T}^{-1}(\mathbf{y}_2)\| \leq C\|\mathbf{y}_1 - \mathbf{y}_2\|, \quad (6)$$

where  $\mathbf{x}_1, \mathbf{x}_2 \in \mathcal{S}_r$  and  $\mathbf{y}_1, \mathbf{y}_2 \in \mathcal{S}$ . The projection operator  $\mathcal{P}(\mathbf{x})$  is defined by composing radial projection  $P_{\mathcal{R}}$  with the Lipschitz continuous mapping  $\mathcal{T}$ . That is,  $\mathcal{P} : B \rightarrow \mathcal{S}$  is

$$\mathcal{P}(\mathbf{x}) = (\mathcal{T} \circ P_{\mathcal{R}})(\mathbf{x}).$$

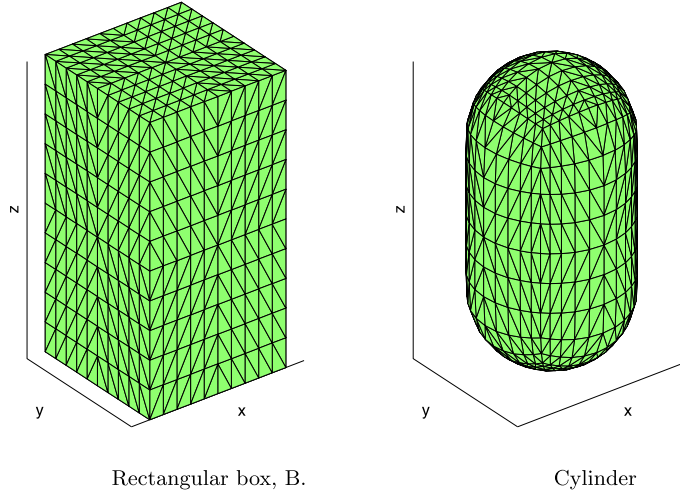


**Fig. 1.** The surface mesh on a cylinder with spherical caps generated by radial projection,  $P_{\mathcal{R}}(\mathbf{x})$  given in (5).

Clearly, the projection operator is also Lipschitz continuous, since it is composed of Lipschitz continuous mappings. The surfaces and meshes generated on closed surfaces such as ellipsoid, dumbbell, heart-shaped surface (and many more) using projection operators are given in Fig. 2. In the following examples, we explicitly give the projection operator  $\mathcal{P}(\mathbf{x})$  used to construct the surfaces plotted in Fig. 2.

#### Ellipsoid

Let  $\mathcal{S}$  be the ellipsoid whose equation is given by  $\frac{x_1^2}{a^2} + \frac{x_2^2}{b^2} + \frac{x_3^2}{c^2} = 1$ , then the projection operator is given by

$$\mathcal{P}(\mathbf{x}) = (\mathcal{T} \circ P_{\mathcal{R}})(\mathbf{x}), \text{ with } \mathcal{T}(x_1, x_2, x_3) = (ax_1, bx_2, cx_3), \text{ where } (x_1, x_2, x_3) \in \mathcal{S}_r.$$

#### Dumbbell

Similarly for a dumbbell, the projection operator  $\mathcal{P}(\mathbf{x})$  is constructed by composing the radial projection with the following Lipschitz continuous mapping:

$$\mathcal{T}(\mathbf{x}) = (x_1, d(x_1)x_2, d(x_1)x_3), \quad \text{where } d(x_1) = \sqrt{1 - a(1 - x_1)^2}, \quad a < 1,$$

where  $(x_1, x_2, x_3) \in \mathcal{S}_r$ .

#### Heart-shaped surface

Let  $\mathcal{S}$  be a heart-shaped surface given by the equation  $(x_1 - x_3^2)^2 + x_2^2 + x_3^2 = 1$ . Then the Lipschitz continuous mapping,  $\mathcal{T}$ , from the sphere onto the heart-shaped surface is given by  $\mathcal{T}(\mathbf{x}) = (x_1 + x_3^2, x_2, x_3)$ . As shown in Fig. 2, various closed surfaces can be constructed by composing the radial projection,  $P_{\mathcal{R}}$ , with a Lipschitz continuous mapping  $\mathcal{T}$ . The following mappings are used for generating the surfaces and meshes for the additional surfaces shown in Fig. 2.

$$\mathcal{T}(x_1, x_2, x_3) = (x_1 - e^{x_3}, x_2 + e^{x_3}, x_3), \quad \text{for Surface I},$$

$$\mathcal{T}(x_1, x_2, x_3) = \left( x_1 + \frac{2x_3}{1+5x_3^2}, x_2 + \frac{2x_3}{1+5x_3^2}, x_3 \right), \quad \text{for Surface II},$$

$$\mathcal{T}(x_1, x_2, x_3) = \left( x_1 + \frac{2x_3^2}{1+5x_3^2}, x_2 + \frac{2x_3^2}{1+5x_3^2}, x_3 \right), \quad \text{for Surface III}.$$

#### Surface mesh generation

Let  $T_h = \{T_i\}_{i=1}^n$  be a triangulation of the surface  $\mathcal{S}$ . A family of triangulation is said to be *shape regular* if there exists a constant  $\kappa > 0$  such that for each  $T_i \in T_h$  we have  $\frac{h_{T_i}}{\rho_{T_i}} < \kappa$ , where  $h_{T_i} = \sup_{\mathbf{y}_1, \mathbf{y}_2 \in T_i} d(\mathbf{y}_1, \mathbf{y}_2)$  and  $\rho_{T_i}$  is the radius of the inscribed circle in  $T_i$ , that is  $\rho_{T_i} = \sup_{\mathbf{y}_0 \in T_i} \inf_{\mathbf{y} \in \partial T_i} d(\mathbf{y}, \mathbf{y}_0)$ . Here  $d(\mathbf{y}_1, \mathbf{y}_2)$  is the distance on the surface which is the length of the shortest curve joining the points  $\mathbf{y}_1$  and  $\mathbf{y}_2$  on  $\mathcal{S}$ . Namely,

$$d(\mathbf{y}_1, \mathbf{y}_2) = \inf\{\mathcal{L}(s) : s \text{ is continuously differentiable curve joining } \mathbf{y}_1 \text{ and } \mathbf{y}_2\}$$

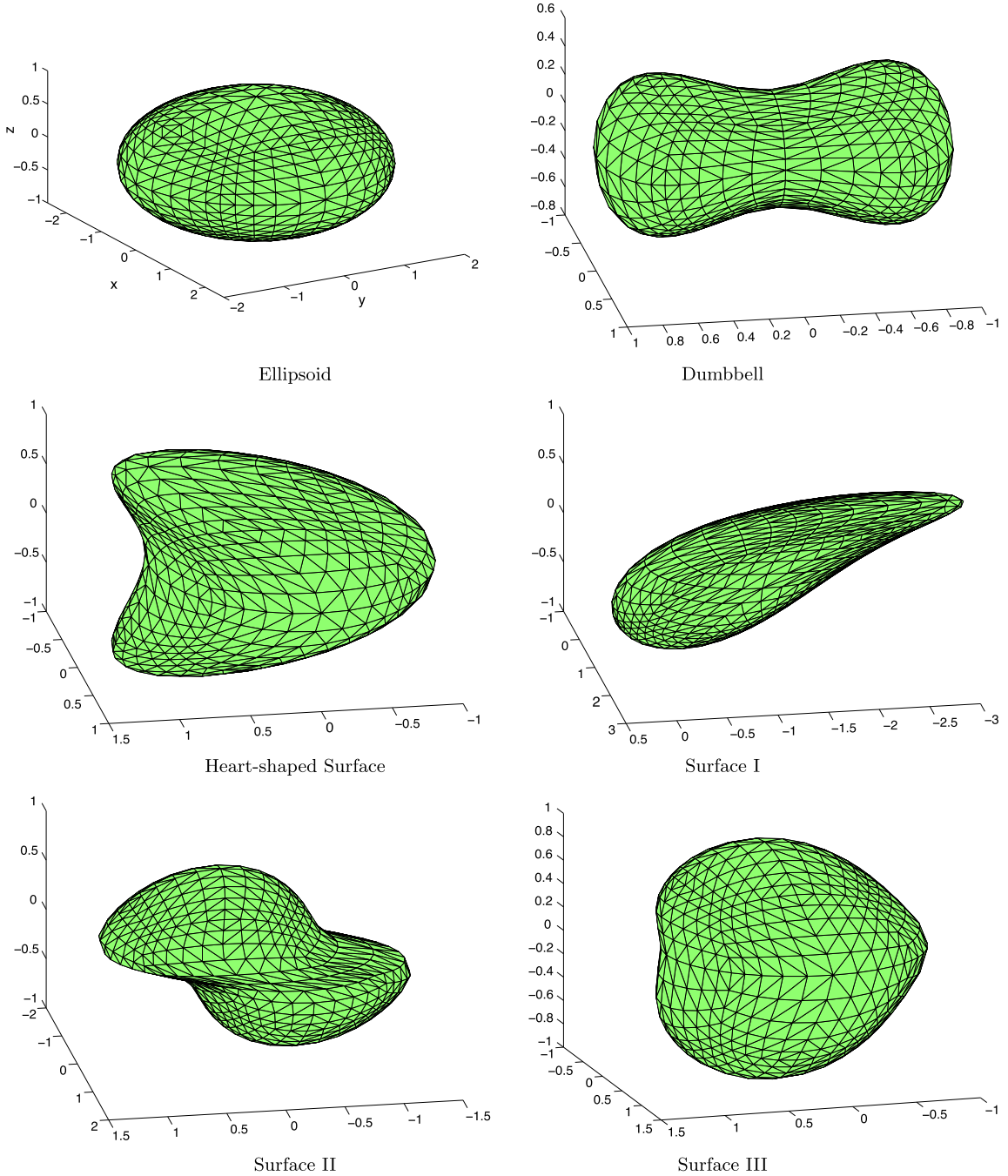


**Fig. 2.** Surfaces and meshes generated by a projection operator,  $\mathcal{P}(\mathbf{x})$ ; ellipsoidal, dumbbell-shaped, heart-shaped and three additional surfaces.

where  $\mathcal{L}(s)$  is the length of the curve  $s$ . Note that for any two points  $\mathbf{y}_1$  and  $\mathbf{y}_2$  on the surface  $\mathcal{S}$  there is an equivalence relationship between the Euclidean distance,  $\|\mathbf{y}_1 - \mathbf{y}_2\|$ , and the geodesic distance,  $d(\mathbf{y}_1, \mathbf{y}_2)$  ([28], Lemma 6.2, page 94). Hence, there exist constants  $c$  and  $C$  such that

$$c\|\mathbf{y}_1 - \mathbf{y}_2\| \leq d(\mathbf{y}_1, \mathbf{y}_2) < C\|\mathbf{y}_1 - \mathbf{y}_2\|. \quad (7)$$

We use the radial projection to generate a mesh on the sphere  $\mathcal{S}_r$  in the following way: Let  $K_h = \{K_i\}_{i=1}^n$  be a shape regular triangulation of the box  $B$ , then a triangulation  $T_h^{\mathcal{S}_r} = \{T_i^{\mathcal{S}_r}\}_{i=1}^n$  of the sphere  $\mathcal{S}_r$  is given by  $T_h^{\mathcal{S}_r} = P_{\mathcal{R}}(K_h)$ . It is proved in [39,52] that the triangulation  $T_h^{\mathcal{S}_r}$  generated by the radial projection,  $P_{\mathcal{R}}$  is shape regular.

We use the projection operator to generate a mesh on the surface  $\mathcal{S}$  in a similar way. Suppose  $K_h = \{K_i\}_{i=1}^n$  is a shape regular triangulation of the box  $B$ , then a triangulation  $T_h = \{T_i\}_{i=1}^n$  of the surface  $\mathcal{S}$  is given by  $T_h = \mathcal{P}(K_h)$ . We denote a planar triangle by  $K_i$  and the corresponding surface triangle by  $T_i$ . That is for any  $\mathbf{x} \in K_i$ , we have  $P(\hat{\mathbf{x}}) = \mathbf{y}$  where  $\mathbf{y} \in T_i$ . In Proposition 1 we prove that the meshes constructed by the projection operators are also shape regular.

**Proposition 1.** Let  $K_h = \{K_i\}_{i=1}^n$  be a shape regular triangulation of the box  $B$  and let  $T_h = \{T_i\}_{i=1}^n$  be the triangulation of the surface  $\mathcal{S}$  such that  $T_h = \mathcal{P}(K_h)$ . Then  $T_h$  is a shape regular triangulation of the surface  $\mathcal{S}$ .

**Proof.** Let  $\mathbf{y}_1$  and  $\mathbf{y}_2$  be two points on the surface triangle  $T_i$  such that  $h_{T_i} = d(\mathbf{y}_1, \mathbf{y}_2)$ . From (7), we obtain,  $d(\mathbf{y}_1, \mathbf{y}_2) < C\|\mathbf{y}_1 - \mathbf{y}_2\|$ . Suppose that  $\mathbf{x}_1$  and  $\mathbf{x}_2$  are on the corresponding planar triangle  $K_i$  and that  $\mathbf{y}_1 = \mathcal{P}(\mathbf{x}_1)$  and  $\mathbf{y}_2 = \mathcal{P}(\mathbf{x}_2)$ . Since the projection operator is Lipschitz continuous, there exists a constant  $c_1$  such that

$$\|\mathbf{y}_1 - \mathbf{y}_2\| = \|\mathcal{P}(\mathbf{x}_1) - \mathcal{P}(\mathbf{x}_2)\| \leq c_1 \|\mathbf{x}_1 - \mathbf{x}_2\|.$$

Hence,  $d(\mathbf{y}_1, \mathbf{y}_2) < C\|\mathbf{y}_1 - \mathbf{y}_2\| \leq Cc_1 \|\mathbf{x}_1 - \mathbf{x}_2\|$ . Thus  $h_{T_i} \leq Cc_1 h_{K_i}$ .

Let  $\mathbf{x}_0$  be the center of the inscribed circle in planar triangle  $K_i$  and set  $\mathbf{y}_0 = \mathcal{P}(\mathbf{x}_0)$ . Let  $c_2$  be the Lipschitz constant of the inverse projection operator  $\mathcal{P}^{-1}$ , then

$$\begin{aligned} \rho_{K_i} &= \inf_{\mathbf{x} \in \partial K_i} \|\mathbf{x} - \mathbf{x}_0\| = \inf_{\mathbf{y} \in \partial T_i} \|\mathcal{P}^{-1}(\mathbf{y}) - \mathcal{P}^{-1}(\mathbf{y}_0)\| \quad \text{since } \mathcal{P}^{-1} \text{ is Lipschitz continuous} \\ &\leq c_2 \inf_{\mathbf{y} \in \partial T_i} \|\mathbf{y} - \mathbf{y}_0\| \quad \text{using (7)} \\ &\leq c_2 \frac{1}{c} \inf_{\mathbf{y} \in \partial T_i} d(\mathbf{y}, \mathbf{y}_0) \leq c_2 \frac{1}{c} \rho_{T_i}. \end{aligned}$$

Hence

$$\frac{h_{T_i}}{\rho_{T_i}} \leq \frac{Cc_1 c_2}{c} \frac{h_{K_i}}{\rho_{K_i}}. \quad \square$$

**Remark 2.** Note that the quality of the mesh depends on the Lipschitz constant of the projection operator  $\mathcal{P}$  and its inverse, since  $\frac{h_{T_i}}{\rho_{T_i}} \leq \frac{Cc_1 c_2}{c} \frac{h_{K_i}}{\rho_{K_i}}$  (see Surface II in Fig. 2 for example).

### 3.2.2. Space and time-discretizations

Before we introduce the finite dimensional subspace  $X$  of the product space  $\mathcal{H}$ , let us first define the finite dimensional subspace  $\chi$  of  $H^1(\mathcal{S})$ . Let  $\mathcal{K} = \{K_i\}_{i=1}^n$  be the triangulation of the surface of the cube  $B$ , then we define the finite element space  $\chi \subset H^1(\mathcal{S})$  as

$$\chi = \left\{ \omega_h : \omega_h = \hat{\omega} \circ \mathcal{P}^{-1} \quad \hat{\omega} \text{ is a continuous piecewise linear polynomial on } B \text{ and } \hat{\omega}|_{K_i} \text{ is linear} \right\}. \quad (8)$$

We then define,  $X = \chi \times \chi$ . Clearly,  $X \subset \mathcal{H}$ . Let  $\{(\varphi_i, 0), (0, \varphi_i)\}_{i=1}^n$  be the basis of  $X$ , then  $(u_h, v_h)$  in  $X$  has a unique representation, given by  $u_h(\mathbf{x}, t) = \sum_{i=1}^n \alpha_{u,i}(t) \varphi_i(\mathbf{x})$  and  $v_h(\mathbf{x}, t) = \sum_{i=1}^n \alpha_{v,i}(t) \varphi_i(\mathbf{x})$ . Thus  $\partial_t u_h(\mathbf{x}, t) = \sum_{i=1}^n \partial_t \alpha_{u,i}(t) \varphi_i(\mathbf{x})$  and  $\partial_t v_h(\mathbf{x}, t) = \sum_{i=1}^n \partial_t \alpha_{v,i}(t) \varphi_i(\mathbf{x})$ . We are now ready to define the semi-discrete weak formulation: Find  $(u_h, v_h) \in X$  such that

$$\begin{cases} (\partial_t u_h, \omega_h) + (\nabla_{\mathcal{S}} u_h, \nabla_{\mathcal{S}} \omega_h) + \gamma(u_h, \omega_h) = \gamma(a + (u_h)^2 v_h, \omega_h), \\ (\partial_t v_h, \nu_h) + d(\nabla_{\mathcal{S}} v_h, \nabla_{\mathcal{S}} \nu_h) = \gamma(b - (u_h)^2 v_h, \nu_h), \end{cases} \quad (9)$$

for all  $(\omega_h, \nu_h) \in X$  a.e.  $t > 0$ .

We obtain the approximate solution of (3) in two steps. First, we discretize in space and get a semi-discrete problem. To obtain a fully discrete problem, we then discretize in time. In the semi-discrete problem (9), we approximate the solution  $(u(\mathbf{x}, t), v(\mathbf{x}, t)) \in L^2(0, T; \mathcal{H})$  by functions  $(u_h(\mathbf{x}, t), v_h(\mathbf{x}, t))$  which, for each fixed time, belong to a finite dimensional space  $X$ . Note that the semi-discrete problem is a system of ordinary differential equations in time. In the second step, we discretize this system in the time variable using finite differences.

For the time discretization let  $T_m$  denote the maximum time of interest,  $\tau$  denote the time step and  $J$  be a fixed nonnegative integer, then  $\tau = \frac{T_m}{J}$  and  $t_k = k\tau$ ,  $k = 0, 1, 2, \dots, J$ . We denote the approximate solution at time  $t_k$  by  $u_h^k =$

$u_h(\cdot, t_k)$ , and  $v_h^k = v_h(\cdot, t_k)$ , thus  $(u_h^k, v_h^k) \in X$ . We approximate the time derivative by the backward Euler difference quotient and denote by  $\bar{\partial}$  the following finite difference operator:

$$\bar{\partial} u_h^{k+1} = \frac{u_h^{k+1} - u_h^k}{\tau}.$$

Employing this difference approximation yields an implicit method resulting in a system of nonlinear algebraic equations. So, the *fully discrete weak formulation* is: Find  $(u_h, v_h) \in X$  such that

$$(\bar{\partial} u_h^{k+1}, \omega_h) + (\nabla_S u_h^{k+1}, \nabla_S \omega_h) + \gamma(u_h^{k+1}, \omega_h) = \gamma(a + (u_h^{k+1})^2 v_h^{k+1}, \omega_h) \quad (10)$$

and

$$(\bar{\partial} v_h^{k+1}, v_h) + d(\nabla_S v_h^{k+1}, \nabla_S v_h) = \gamma(b - (u_h^{k+1})^2 v_h^{k+1}, v_h), \quad (11)$$

for all  $(\omega_h, v_h) \in X$ . That is given the approximate solution at time  $k$ , we obtain an approximation to the solution at time  $k+1$  by solving the nonlinear system given by equations (10) and (11).

**Remark 3.** The resulting system of nonlinear algebraic equations is solved by use of the Picard iteration. Alternatively, Newton's method can be used at the expense of computing derivatives. We consider this method in future studies. One could also use a modified backward Euler method as proposed by Madzvamuse [35].

Using the Picard iteration, an approximate solution of (10) and (11) can be obtained by performing several iterations in the following way: for  $l = 1, \dots, N$ , solve

$$\frac{1}{\tau}(\bar{u}_h^{l+1}, \omega_h) + (\nabla_S \bar{u}_h^{l+1}, \nabla_S \omega_h) + \gamma(\bar{u}_h^{l+1}, \omega_h) - \gamma(a + (\bar{u}_h^l)^2 \bar{v}_h^l, \omega_h) = \frac{1}{\tau}(u_h^k, \omega_h) \quad (12)$$

and

$$\frac{1}{\tau}(\bar{v}_h^{l+1}, v_h) + d(\nabla_S \bar{v}_h^{l+1}, \nabla_S v_h) - \gamma(b - (\bar{u}_h^l)^2 \bar{v}_h^l, v_h) = \frac{1}{\tau}(\bar{v}_h^l, v_h), \quad (13)$$

for all  $(\omega_h, v_h) \in X$ , where  $\bar{u}_h^{l+1}$  and  $\bar{v}_h^{l+1}$  are approximations to  $u_h^{k+1}$  and  $v_h^{k+1}$ . Here  $l$  denotes the index for Picard's iteration (and not the time level). Let  $\alpha_u^k$  and  $\alpha_v^k$  denote the vector of nodal values at time  $t_k$  for  $u$  and  $v$  respectively, and similarly let  $\bar{\alpha}_u^l$  and  $\bar{\alpha}_v^l$  denote the vector of nodal values at the Picard iteration  $l$  for  $u$  and  $v$  respectively, then (12) and (13) lead to the following system

$$\begin{cases} \bar{M}\bar{\alpha}_u^{l+1} + \tau\bar{G}\bar{\alpha}_u^{l+1} + \tau\gamma\bar{M}\bar{\alpha}_u^{l+1} = \bar{M}\alpha_u^k + \tau\gamma f^l, \\ \bar{M}\bar{\alpha}_v^{l+1} + \tau\bar{D}\bar{G}\bar{\alpha}_v^{l+1} = \bar{M}\alpha_v^k + \tau\gamma g^l, \end{cases} \quad (14)$$

where  $\bar{M}$  is the mass matrix with components  $\bar{M}_{ij} = (\varphi_j, \varphi_i)$ ,  $\bar{G}$  is the stiffness matrix with  $\bar{G}_{ij} = (\nabla_S \varphi_j, \nabla_S \varphi_i)$  and the right hand side vectors are  $(f^l)_j = (a + (\bar{u}_h^l)^2 \bar{v}_h^l, \varphi_j)$  and  $(g^l)_j = (b - (\bar{u}_h^l)^2 \bar{v}_h^l, \varphi_j)$ . Setting  $\bar{\alpha}^l = \begin{bmatrix} \bar{\alpha}_u^l \\ \bar{\alpha}_v^l \end{bmatrix}$  and similarly  $\alpha^k = \begin{bmatrix} \alpha_u^k \\ \alpha_v^k \end{bmatrix}$ , system (14) can be rewritten as

$$\bar{\alpha}^{l+1} = (M + \tau\mathcal{D}G + \tau\gamma M_u)^{-1} \left( \tau\gamma F(\bar{\alpha}^l) + M\alpha^k \right) \quad (15)$$

where  $M = \begin{bmatrix} \bar{M} & 0 \\ 0 & \bar{M} \end{bmatrix}$  is a block diagonal matrix whose blocks are the mass matrix  $\bar{M}$  and  $M_u = \begin{bmatrix} \bar{M} & 0 \\ 0 & 0 \end{bmatrix}$ . The matrix  $G = \begin{bmatrix} \bar{G} & 0 \\ 0 & \bar{G} \end{bmatrix}$  is a block diagonal matrix whose blocks are the stiffness matrix  $\bar{G}$ . The vector  $F(\bar{\alpha}^l) = \begin{bmatrix} f^l \\ g^l \end{bmatrix}$  is a block vector and  $\mathcal{D} = \begin{bmatrix} 1 & 0 \\ 0 & d \end{bmatrix}_{2 \times 2}$  is the diffusivity tensor with diffusion constants on the diagonal.

### 3.3. Implementation of the projected finite element method and its approximation properties

#### 3.3.1. Implementing projected finite element method

The projected finite element method provides exact triangulation of the surface and this leads to a conforming finite element discretization. All the computations are done on the surface of the cube which is embedded in  $\mathbb{R}^3$ , hence the projected finite element method yields a “logically” rectangular discretization. We choose the term “logically” rectangular to describe the projected finite element discretization since all the nodes at the surface of the cube are the vertices of a lattice (see Fig. 3).

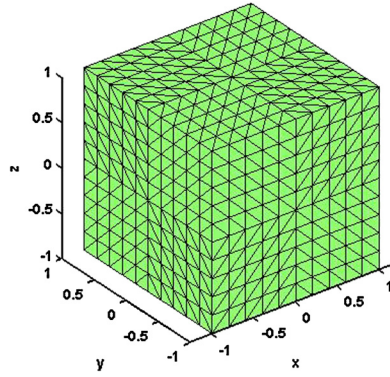


**Fig. 3.** Uniform mesh on the surface of the cube,  $B$ .

We start with a uniform triangulation of the surface of the cube  $B$  (see Fig. 3). Let  $K$  denote a planar triangle on the surface of the cube. Note that the triangles are flat but embedded in  $\mathbb{R}^3$ . Thus, the nodes  $\{\hat{\eta}_i\}_{i=1}^3$  of the planar triangle  $K$  are in  $\mathbb{R}^3$ . Let  $\{\hat{\varphi}_i\}_{i=1}^3$  be the linear basis functions for the planar triangle  $K$ , which satisfy  $\hat{\varphi}_i(\hat{\eta}_j) = \delta_{ij}$  where  $\delta_{ij} = \begin{cases} 0 & \text{if } i=j, \\ 1 & \text{if } i \neq j. \end{cases}$  For notational convenience let a point on  $\mathbf{x} \in K$  be represented by  $\mathbf{x} = (x_1, x_2, x_3)$ , and a point  $\mathbf{y}$  on the surface triangle  $T$  be represented by  $\mathbf{y} = (y_1, y_2, y_3)$ . Thus the projection operator  $\mathcal{P}$  will project the planar triangle  $K$  onto the surface triangle  $T$ ,  $\mathcal{P}(\mathbf{x}) = \mathbf{y}$  where

$$\mathcal{P}(x_1, x_2, x_3) = (y_1(x_1, x_2, x_3), y_2(x_1, x_2, x_3), y_3(x_1, x_2, x_3)) = (y_1, y_2, y_3).$$

The inverse projection maps the surface triangle  $T$  onto the planar triangle  $K$ ,  $\mathcal{P}^{-1}(\mathbf{y}) = \mathbf{x}$ . Thus

$$\mathcal{P}^{-1}(y_1, y_2, y_3) = (x_1(y_1, y_2, y_3), x_2(y_1, y_2, y_3), x_3(y_1, y_2, y_3)) = (x_1, x_2, x_3).$$

In all our computations, we take a cube whose  $\|\mathbf{x}\|_\infty = 1$ , which is the unit circle with respect to the infinity norm. We denote the faces of the cube by Face 1, Face 2, ..., Face 6. We project the surface of the cube onto the surface,  $S$  by the projection operator,  $\mathcal{P}$ . For example, the projection operator from the surface of the cube onto the heart-shaped surface (as shown in Fig. 2) is as the following

$$\mathcal{P}(\mathbf{x}) = \left( \frac{x_1\sqrt{x_1^2 + x_2^2 + x_3^2} + x_3^2}{x_1^2 + x_2^2 + x_3^2}, \frac{x_2}{\sqrt{x_1^2 + x_2^2 + x_3^2}}, \frac{x_3}{\sqrt{x_1^2 + x_2^2 + x_3^2}} \right). \quad (16)$$

Clearly, the projection operator  $\mathcal{P}(\mathbf{x})$  in (16) is not one-to-one. But, restricted to each face the projection operator is one-to-one and onto. Hence the inverse  $\mathcal{P}^{-1}$  is well defined. The inverse of the projection operator in (16) restricted to each face of the cube is given by

$$\begin{aligned} \mathcal{P}_1^{-1}(\mathbf{y}) &= \left( 1, \frac{y_2}{y_1 - y_3^2}, \frac{y_3}{y_1 - y_3^2} \right) && \text{projects onto Face 1 } \mathbf{x} = (1, x_2, x_3), \\ \mathcal{P}_2^{-1}(\mathbf{y}) &= \left( \frac{y_1 - y_3^2}{y_2}, 1, \frac{y_3}{y_2} \right) && \text{projects onto Face 2 } \mathbf{x} = (x_1, 1, x_3), \\ \mathcal{P}_3^{-1}(\mathbf{y}) &= \left( -1, \frac{-y_2}{y_1 - y_3^2}, \frac{-y_3}{y_1 - y_3^2} \right) && \text{projects onto Face 3 } \mathbf{x} = (-1, x_2, x_3), \\ \mathcal{P}_4^{-1}(\mathbf{y}) &= \left( \frac{-y_1 + y_3^2}{y_1}, -1, \frac{-y_3}{y_2} \right) && \text{projects onto Face 4 } \mathbf{x} = (x_1, -1, x_3), \\ \mathcal{P}_5^{-1}(\mathbf{y}) &= \left( \frac{-y_1 + y_3^2}{y_3}, \frac{-y_2}{y_3}, -1 \right) && \text{projects onto Face 5 } \mathbf{x} = (x_1, x_2, -1), \\ \mathcal{P}_6^{-1}(\mathbf{y}) &= \left( \frac{y_1 - y_3^2}{y_3}, \frac{y_2}{y_3}, 1 \right) && \text{projects onto Face 6 } \mathbf{x} = (x_1, x_2, 1). \end{aligned}$$

The basis functions on the surface triangle,  $T$  are constructed by

$$\varphi_i = \hat{\varphi}_i \circ \mathcal{P}^{-1}, \quad i = 1, 2, 3, \quad (17)$$

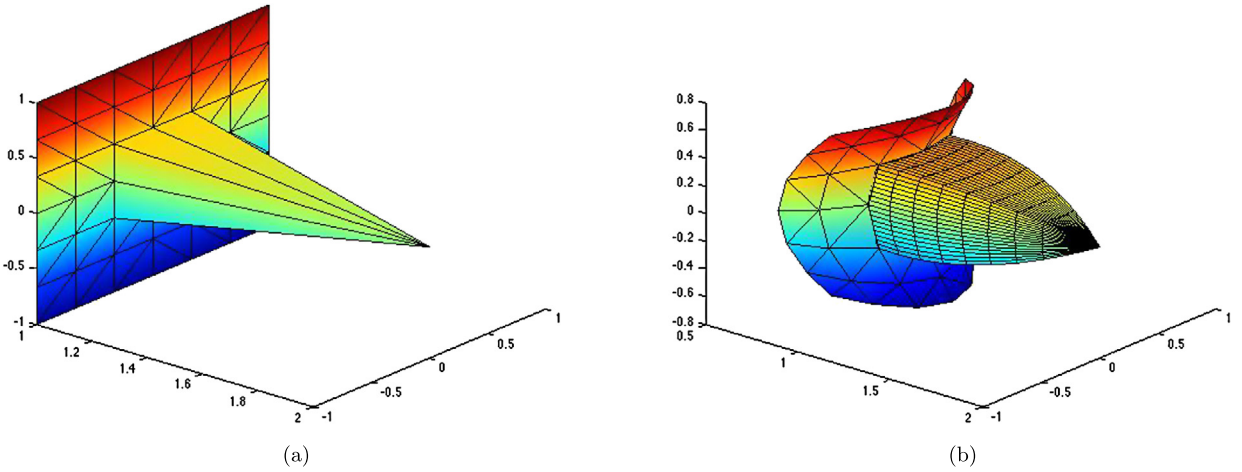


**Fig. 4.** (a) A linear basis function  $\hat{\varphi}_i$  on the Face 1 ( $x = (1, x_2, x_3)$ ) of the cube. (b) Corresponding basis function constructed by  $\varphi_i = \hat{\varphi}_i \circ \mathcal{P}^{-1}$  and the projection of Face 1 onto the heart-shaped surface.

where  $\hat{\varphi}_i$  are the linear basis functions on the planar triangle  $K$  with  $\mathcal{P}(K) = T$  (see (8)). Note that the basis functions on surface triangles are not linear, but rational functions. In Fig. 4 (a), a linear basis function on Face 1 of the cube is plotted. In Fig. 4 (b) the corresponding basis function and the projection of the Face 1 onto the heart-shaped surface by (16) are shown.

Components of the mass matrix  $\bar{M}_{ij} = (\varphi_j, \varphi_i)$  are computed on the planar triangles by use of change of variables in the following way

$$\begin{aligned} (\varphi_j, \varphi_i) &= \int_{\mathcal{S}} \varphi_i \varphi_j = \sum_T \int_T \varphi_i \varphi_j \quad \text{by definition (17)} \\ &= \sum_T \int_T (\hat{\varphi}_i \circ \mathcal{P}^{-1}) (\hat{\varphi}_j \circ \mathcal{P}^{-1}) \quad \text{by change of variables} \\ &= \sum_K \int_K \hat{\varphi}_i \hat{\varphi}_j |\bar{J}|. \end{aligned}$$

In the above,  $|\bar{J}|$  is the determinant of the Jacobian matrix  $\bar{J}$ . The matrix  $\bar{J}$  is the Jacobian of the projection operator  $\mathcal{P} : B \rightarrow \mathcal{S}$  which is given by

$$\bar{J} = \begin{bmatrix} \frac{\partial y_1}{\partial x_1} & \frac{\partial y_1}{\partial x_2} & \frac{\partial y_1}{\partial x_3} \\ \frac{\partial y_2}{\partial x_1} & \frac{\partial y_2}{\partial x_2} & \frac{\partial y_2}{\partial x_3} \\ \frac{\partial y_3}{\partial x_1} & \frac{\partial y_3}{\partial x_2} & \frac{\partial y_3}{\partial x_3} \\ \frac{\partial y_1}{\partial x_1} & \frac{\partial y_1}{\partial x_2} & \frac{\partial y_1}{\partial x_3} \end{bmatrix}.$$

To compute the components of the stiffness matrix  $\bar{G}$ , we again use a transformation of variables. The tangential derivatives of the basis functions are by definition equal to

$$\nabla_{\mathcal{S}} \varphi_i = \nabla \varphi_i - (\nabla \varphi_i \cdot \mathbf{n}) \mathbf{n}, \quad (18)$$

where  $\mathbf{n} = \mathbf{n}(y_1, y_2, y_3)$  is the normal to the surface  $\mathcal{S}$  and  $\nabla \varphi_i = (\frac{\partial \varphi_i}{\partial y_1}, \frac{\partial \varphi_i}{\partial y_2}, \frac{\partial \varphi_i}{\partial y_3})$ . The equation of the heart-shaped surface obtained by the projection operator  $\mathcal{P}$  in (16) is  $(y_1 - y_3^2)^2 + y_2^2 + y_3^2 = 1$ . Hence, the normal to the heart-shaped surface is

$$\mathbf{n}(\mathbf{y}) = \left( y_1 - y_3^2, y_2, y_3(1 - 2(y_1 - y_3^2)) \right) / \sqrt{1 + 4y_2^2(1 - y_1 - y_2^2)}.$$

Since the basis functions on the surface triangle are constructed by composing the linear basis functions of the planar triangle with the inverse projection, we have

$$\nabla \varphi_i = \bar{J}^T \nabla \hat{\varphi}_i, \quad (19)$$

where  $\nabla \hat{\varphi}_i = \left( \frac{\partial \hat{\varphi}_i}{\partial x_1}, \frac{\partial \hat{\varphi}_i}{\partial x_2}, \frac{\partial \hat{\varphi}_i}{\partial x_3} \right)$  and  $\bar{J}^T$  is the transpose of Jacobian of the inverse projection  $\mathcal{P}^{-1} : \mathcal{S} \rightarrow B$ . Note that since the inverse projection is different for each face of the cube, the matrix  $\bar{J}^T$  is computed based on the location of the planar triangle on the cube. For instance, the transposed Jacobian of the inverse projection of heart-shaped surface,  $\mathcal{P}_1^{-1}(\mathbf{x})$ , onto Face 1 is

$$\bar{J}^T = \begin{bmatrix} \frac{\partial x_1}{\partial y_1} & \frac{\partial x_2}{\partial y_1} & \frac{\partial x_3}{\partial y_1} \\ \frac{\partial x_1}{\partial y_2} & \frac{\partial x_2}{\partial y_2} & \frac{\partial x_3}{\partial y_2} \\ \frac{\partial x_1}{\partial y_3} & \frac{\partial x_2}{\partial y_3} & \frac{\partial x_3}{\partial y_3} \end{bmatrix} = \begin{bmatrix} 1 & \frac{-y_2}{(y_1 - y_3^2)^2} & \frac{-y_3}{(y_1 - y_3^2)^2} \\ 0 & \frac{1}{y_1 - y_3^2} & 0 \\ 0 & \frac{2y_2y_3}{(y_1 - y_3^2)^2} & \frac{y_1 + y_3^2}{(y_1 - y_3^2)^2} \end{bmatrix}$$

We then compute the components of the stiffness matrix in the following way

$$\begin{aligned} \bar{G}_{ij} &= (\nabla_{\mathcal{S}} \varphi_j, \nabla_{\mathcal{S}} \varphi_i) = \int_{\mathcal{S}} \nabla_{\mathcal{S}} \varphi_i \cdot \nabla_{\mathcal{S}} \varphi_j \\ &= \sum_T \int_T (\nabla \varphi_i - (\nabla \varphi_i \cdot \mathbf{n}) \mathbf{n}) \cdot (\nabla \varphi_j - (\nabla \varphi_j \cdot \mathbf{n}) \mathbf{n}) \quad \text{since } \nabla \varphi_i = \bar{J}^T \nabla \hat{\varphi}_i \\ &= \sum_K \int_K \left( \bar{J}^T \nabla \hat{\varphi}_i - \left( \bar{J}^T \nabla \hat{\varphi}_i \cdot \mathbf{n}(\mathcal{P}(\mathbf{x})) \right) \mathbf{n}(\mathcal{P}(\mathbf{x})) \right) \cdot \left( \bar{J}^T \nabla \hat{\varphi}_j - \left( \bar{J}^T \nabla \hat{\varphi}_j \cdot \mathbf{n}(\mathcal{P}(\mathbf{x})) \right) \mathbf{n}(\mathcal{P}(\mathbf{x})) \right) |\bar{J}|. \end{aligned}$$

In the above, we have used the definition of the tangential derivative and change of variables appropriately. Thus all the integrals are computed exactly on the surface of the cube  $B$ . Since the projected finite element method is based on mapping a three dimensional cube onto the surface  $\mathcal{S}$ , we transform the surface gradients  $\nabla_{\mathcal{S}} \varphi_i$  to the surface of the cube by

$$\nabla_{\mathcal{S}} \varphi_i = \bar{J}^T \nabla \hat{\varphi}_i - \left( \bar{J}^T \nabla \hat{\varphi}_i \cdot \mathbf{n}(\mathcal{P}(\mathbf{x})) \right) \mathbf{n}(\mathcal{P}(\mathbf{x})). \quad (20)$$

Note that the transformation of the tangential derivative to the surface of the cube is equivalent to the definition of the surface gradient in classic differential geometry in the following way. If we restrict the projection operator to the faces of the cube, then it can be considered as a mapping from a unit square in two dimensions to a surface in three dimensions. For example, for the case of heart-shaped surface, if we restrict the projection operator to Face 1, then the projection operator is equivalent to the following map from the unit square, denoted by  $\hat{U}$ , in  $\mathbb{R}^2$  to a portion of the heart-shaped surface, denoted by  $\hat{\mathcal{S}}$ , in  $\mathbb{R}^3$  (see Fig. 4 (b))

$$\hat{X}(u_1, u_2) = \left( \frac{\sqrt{1 + u_1^2 + u_2^2} + u_2^2}{1 + u_1^2 + u_2^2}, \frac{u_1}{\sqrt{1 + u_1^2 + u_2^2}}, \frac{u_2}{\sqrt{1 + u_1^2 + u_2^2}} \right), \text{ for } (u_1, u_2) \in \hat{U},$$

where  $\hat{U} = \{-1 \leq u_1 \leq 1, -1 \leq u_2 \leq 1\}$ . That is the surface  $\hat{\mathcal{S}}$  is parametrized by  $\hat{X} : \hat{U} \rightarrow \hat{\mathcal{S}}$ .

Let  $T(\hat{\mathcal{S}})$  denote the tangent space to the surface  $\hat{\mathcal{S}}$  at a given point. The parametrization  $\hat{X}$  defines a basis  $\{\hat{X}_{u_1}, \hat{X}_{u_2}\}$  of  $T(\hat{\mathcal{S}})$ , where

$$\hat{X}_{u_1} = \frac{\partial \hat{X}}{\partial u_1} \text{ and } \hat{X}_{u_2} = \frac{\partial \hat{X}}{\partial u_2}.$$

Then the first fundamental form of the surface  $\hat{\mathcal{S}}$  is given by

$$\mathcal{I} = E du_1^2 + 2F du_1 du_2 + G du_2^2,$$

where  $du_1$  and  $du_2$  are the differentials with respect to  $u_1$  and  $u_2$  and

$$E = \hat{X}_{u_1} \cdot \hat{X}_{u_1}, \quad F = \hat{X}_{u_1} \cdot \hat{X}_{u_2}, \quad G = \hat{X}_{u_2} \cdot \hat{X}_{u_2}.$$

Let  $\hat{h}$  be a real-valued function defined on the unit square  $\hat{h} : \hat{U} \rightarrow \mathbb{R}$ , then  $h = \hat{h} \circ \hat{X}^{-1}$  is a real valued function defined on the surface  $\hat{\mathcal{S}}$ ,  $h : \hat{\mathcal{S}} \rightarrow \mathbb{R}$ . The tangential derivative of  $h$  in local coordinates is then given by [12]

$$\nabla_{\hat{\mathcal{S}}} h = (\hat{X}_{u_1}, \hat{X}_{u_2}) g^{-1} \begin{pmatrix} \frac{\partial \hat{h}}{\partial \hat{u}_1} \\ \frac{\partial \hat{h}}{\partial \hat{u}_2} \end{pmatrix}, \quad (21)$$

where  $g = \begin{pmatrix} E & F \\ F & G \end{pmatrix}$  and  $g^{-1}$  is the inverse of  $g$ . It can be shown that the transformation of the tangential gradient to the surface of the cube as given in (20) is equivalent to (21).

### 3.3.2. Numerical integration

We use a 13-point Gaussian quadrature rule to approximate integrals on the planar triangles  $K$  [14]. The 13-point quadrature rule used in the computations is as follows;

$$\int_K \hat{u} \approx \text{Area}(K) \sum_{i=1}^{13} \omega_i \hat{u}(\hat{x}_i, \hat{y}_i, \hat{z}_i), \quad (22)$$

where  $\omega_i$  are the weight of the quadrature rule. This quadrature rule is exact for polynomials of degree 7 [14]. The integral over the surface  $\mathcal{S}$  is computed in the following way

$$\begin{aligned} \int_{\mathcal{S}} f(\mathbf{y}) &= \sum_{i=1}^{N_e} \int_{T_i} f(\mathbf{y}) = \sum_{i=1}^{N_e} \int_{K_i} f(\mathcal{P}(\mathbf{x})) |\vec{J}| \\ &= \sum_{i=1}^{N_e} \text{Area}(K_i) \sum_{j=1}^{13} w_j f(\mathcal{P}(\mathbf{x}_j)) |\vec{J}|, \end{aligned} \quad (23)$$

where  $N_e$  is the number of surface triangles.

### 3.3.3. Approximation properties

The following lemma (Lemma 1) has been proved for the radial projection  $P_{\mathcal{R}}$  in [39]. In this paper, we will demonstrate the proof for the projection operator  $\mathcal{P}(\mathbf{x}) = (\mathcal{T} \circ P_{\mathcal{R}})(\mathbf{x})$ . Let  $U$  be an open subset of  $\mathbb{R}^{N+1}$  which contains the surface  $\mathcal{S}$  and  $B$ , we then extend a function  $u : \mathcal{S} \rightarrow \mathbb{R}$  to the open subset  $U$  and denote the extension as  $\hat{u} : U \rightarrow \mathbb{R}$ . We define the extension  $\hat{u}$  with the following properties

$$u(\mathbf{y}) = \hat{u}(\mathbf{y}) \quad \text{and} \quad \nabla_{\mathcal{S}} u(\mathbf{y}) = \nabla \hat{u}(\mathbf{y}), \quad \forall \mathbf{y} \in \mathcal{S}. \quad (24)$$

That is, we extend  $u$  defined on the surface  $\mathcal{S}$  to an open subset  $U$  of  $\mathbb{R}^{N+1}$  such that the extension  $\hat{u}$  is constant in the normal direction to the surface  $\mathcal{S}$ , and varies only along the surface.

**Lemma 1.** Let  $u : \mathcal{S} \rightarrow \mathbb{R}$  and  $\hat{u} : U \rightarrow \mathbb{R}$  be the extension of  $u$  as defined in (24) let  $K$  be a planar triangle on  $B$  and let  $T$  be a surface triangle on  $\mathcal{S}$ , which is obtained by  $T = \mathcal{P}(K)$ , then there exist constants  $c > 0$  and  $C > 0$  such that

- (i)  $c\|\hat{u}\|_{L^2(K)} \leq \|u\|_{L^2(T)} \leq C\|\hat{u}\|_{L^2(K)}$ ,
- (ii)  $c\|\hat{u}\|_{H^1(K)} \leq \|u\|_{H^1(T)} \leq C\|\hat{u}\|_{H^1(K)}$ , (implying the equivalence of norms), and
- (iii)  $|\hat{u}|_{H^2(K)} \leq c\|u\|_{H^2(T)}$
- (iv)  $c\|\nabla \hat{u}\|_{L^2(K)} \leq \|\nabla_{\mathcal{S}} u\|_{L^2(T)} \leq C\|\nabla \hat{u}\|_{L^2(K)}$ .

#### Proof.

(i) Let  $\vec{J}$  be the Jacobian of the projection operator  $\mathcal{P}(\mathbf{x})$ , and  $\vec{J}$  be the Jacobian of the inverse projection operator  $\mathcal{P}^{-1}(\mathbf{x})$ .

Since the projection operator  $\mathcal{P}$  and its inverse  $\mathcal{P}^{-1}$  are Lipschitz continuous, there exist constants  $c$  and  $C$  such that

$$|\vec{J}| \leq C \text{ and } |\vec{J}| \leq \frac{1}{c}. \text{ Hence}$$

$$\|u\|_{L^2(T)}^2 = \int_T |u|^2 = \int_K |u \circ P|^2 |\vec{J}| \leq C \int_K |\hat{u}|^2 = C\|\hat{u}\|_{L^2(K)}^2.$$

Similarly we have

$$\|\hat{u}\|_{L^2(K)}^2 = \int_K |\hat{u}|^2 = \int_T |u \circ P^{-1}|^2 |\vec{J}| \leq \frac{1}{c} \int_T |u|^2 = \frac{1}{c} \|u\|_{L^2(T)}^2.$$

(iv) Note that for any  $\mathbf{x} \in K$ , we have  $P(\mathbf{x}) = \mathbf{y}$  where  $\mathbf{y} \in T$ . Thus by the chain rule we have

$$\nabla \hat{u}(\mathbf{x}) = \vec{J}^T \nabla u(\mathbf{y}), \quad \text{and} \quad \nabla \hat{u}(\mathbf{y}) = \vec{J}^T \nabla \hat{u}(\mathbf{x}), \quad (25)$$

where  $\vec{J}^T$  is the transposed Jacobian of the projection operator  $\mathcal{P}$  and  $\vec{J}^T$  is the transposed Jacobian of the inverse projection operator  $\mathcal{P}^{-1}$ . Thus

$$\begin{aligned}\|\nabla_{\mathcal{S}} u\|_{L^2(T)}^2 &= \int_T |\nabla_{\mathcal{S}} u(\mathbf{y})|^2 = \int_T |\nabla \hat{u}(\mathbf{y})|^2 = \int_K |\vec{J}^T \nabla \hat{u}(\mathbf{x})|^2 |\vec{J}| \\ &\leq C \int_K |\nabla \hat{u}(\mathbf{x})|^2 = C \|\nabla \hat{u}\|_{L^2(K)}^2.\end{aligned}$$

Similarly

$$\|\nabla \hat{u}\|_{L^2(K)}^2 = \int_K |\nabla \hat{u}(\mathbf{x})|^2 = \int_T |\vec{J}^T \nabla \hat{u}(\mathbf{y})|^2 |\vec{J}| \leq \frac{1}{c} \int_T |\nabla \hat{u}(\mathbf{y})|^2 = \frac{1}{c} \|\nabla_{\mathcal{S}} u\|_{L^2(T)}^2.$$

(ii) Consequence of (i) and (iv).

(iii) Taking gradient of  $\nabla \hat{u}(\mathbf{x}) = \vec{J}^T \nabla \hat{u}(\mathbf{y})$  results in

$$\begin{aligned}\nabla^2 \hat{u}(\mathbf{x}) &= \nabla (\vec{J}^T \nabla \hat{u}(\mathbf{y})) \\ &= \nabla (\vec{J}^T) \nabla \hat{u}(\mathbf{y}) + \vec{J}^T \nabla (\nabla \hat{u}(\mathbf{y})) \quad \text{since } \nabla \hat{u}(\mathbf{y}) = \nabla_{\mathcal{S}} u(\mathbf{y}) \\ &= \nabla (\vec{J}^T) \nabla_{\mathcal{S}} u(\mathbf{y}) + \vec{J}^T \nabla (\nabla_{\mathcal{S}} u(\mathbf{y})) \quad \text{using the definition of tangential derivative} \\ &= \nabla (\vec{J}^T) \nabla_{\mathcal{S}} u(\mathbf{y}) + \vec{J}^T \nabla_{\mathcal{S}}^2 u(\mathbf{y}) + \vec{J}^T (\nabla (\nabla_{\mathcal{S}} u(\mathbf{y}) \cdot \mathbf{n}) \mathbf{n}).\end{aligned}$$

Therefore, for some constant  $c$ , we have  $|\hat{u}|_{H^2(K)} \leq c \|u\|_{H^2(T)}$ .  $\square$

Next, we show some approximation properties of the space  $\chi$ . Define the piecewise interpolant  $I_h u \in \chi$  of a function  $u \in C(\mathcal{S})$  by  $I_h u(\eta_i) = u(\eta_i)$ ,  $i = 1, 2, \dots, n$ , where  $\{\eta_i\}_i^n$  are the nodes of the triangulation  $\mathcal{T}_h$ .

**Proposition 2.** For any function  $u$  defined on a surface triangle  $T$ , in which  $T = P(K)$ , we have  $\hat{u}|_K = u \circ \mathcal{P}|_K$ . Then the restriction of the interpolation to the planar triangle  $K$  is  $I_K \hat{u} = (I_h u \circ \mathcal{P})|_K$ , where  $I_K$  is the piecewise linear interpolation of  $\hat{u}$  on the planar triangle  $K$ .

**Proof.** Let  $\{\varphi_i\}_{i=1}^3$  be the projected finite element basis functions associated with the surface triangle  $T$ , and let  $\{\eta_i\}_{i=1}^3$  be the vertices of the surface triangle  $T$ . Since  $T = P(K)$ , we have  $\eta_i = \mathcal{P}(\hat{\eta}_i)$ ,  $i = 1, 2, 3$ , where  $\{\hat{\eta}_i\}_{i=1}^3$  are the vertices of the planar triangle  $K$ . Let  $\{\hat{\varphi}_i\}_{i=1}^3$  be the linear finite element basis functions of the planar triangle  $K$ , then by definition we have  $\varphi_i = \hat{\varphi}_i \circ \mathcal{P}^{-1}$ ,  $i = 1, 2, 3$ . Let  $u \in C(T)$ , then  $I_h u = \sum_{i=1}^3 u(\eta_i) \varphi_i$ . Composing both sides with  $\mathcal{P}$ , we get

$$\begin{aligned}I_h u \circ P &= \sum_{i=1}^3 u(\eta_i) \varphi_i \circ \mathcal{P} \quad \text{since } \eta_i = \mathcal{P}(\hat{\eta}_i) \text{ and } \varphi_i = \hat{\varphi}_i \circ \mathcal{P}^{-1} \\ &= \sum_{i=1}^3 u(\mathcal{P}(\hat{\eta}_i)) \hat{\varphi}_i = \sum_{i=1}^3 \hat{u}(\hat{\eta}_i) \hat{\varphi}_i = I_K \hat{u}.\end{aligned}$$

We set  $I_K \hat{u} = (I_h u \circ \mathcal{P})|_K$ .  $\square$

The following estimates are well known consequences of the Bramble–Hilbert lemma (see [3,4,8,27], for details)

$$\|I_K \hat{u} - \hat{u}\|_{L^2(K)} \leq ch^2 |\hat{u}|_{H^2(K)} \tag{26}$$

and

$$\|\nabla(I_K \hat{u} - \hat{u})\|_{L^2(K)} \leq ch |\hat{u}|_{H^2(K)}. \tag{27}$$

**Theorem 1.** Let  $u \in H^2(\mathcal{S})$  and let  $I_h u \in \chi$  be the interpolant of  $u$ , then

$$\|I_h u - u\|_{L^2(\mathcal{S})} \leq ch^2 \|u\|_{H^2(\mathcal{S})} \tag{28}$$

and

$$\|\nabla_{\mathcal{S}}(I_h u - u)\|_{L^2(\mathcal{S})} \leq ch \|u\|_{H^2(\mathcal{S})}. \tag{29}$$

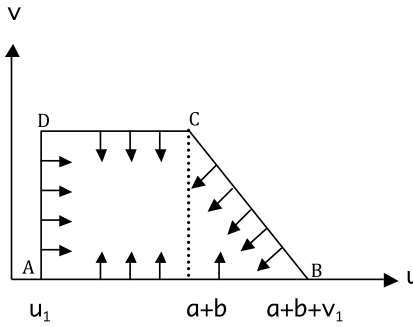


**Fig. 5.** The invariant region  $\mathcal{I}$  bounded by the quadrilateral  $ABCPA$ .

**Proof.** We only prove inequality (28), since the proof of inequality (29) is similar. Since for any  $u$  defined on the surface triangle  $T$ , we have that  $\hat{u}|_K = u \circ \mathcal{P}|_K$ , using Lemma 1 we get that

$$\|I_h u - u\|_{L^2(\mathcal{S})}^2 = \sum_T \|I_h u - u\|_{L^2(T)}^2 \leq C \sum_K \|I_h u \circ \mathcal{P} - u \circ \mathcal{P}\|_{L^2(K)}^2.$$

Since  $I_K \hat{u} = (I_h u \circ \mathcal{P})|_K$ , using (26) we get that

$$\begin{aligned} \|I_h u - u\|_{L^2(\mathcal{S})}^2 &\leq C \sum_K \|I_K \hat{u} - \hat{u}\|_{L^2(K)}^2 \\ &\leq C \sum_K h^4 |\hat{u}|_{H^2(K)}^2 \quad \text{by Lemma 1} \\ &\leq C \sum_T h^4 \|u\|_{H^2(T)}^2. \end{aligned}$$

Hence

$$\|I_h u - u\|_{L^2(\mathcal{S})} \leq Ch^2 \|u\|_{H^2(\mathcal{S})}. \quad \square$$

**Remark 4.** Note that Theorem 1 is a result of the fact that the projection operator  $\mathcal{P}$  and its inverse  $\mathcal{P}^{-1}$  are Lipschitz continuous. Clearly the interpolant  $I_h u$  is well defined for continuous functions, since it uses the nodal values of the function  $u$ . Since  $u \in H^2(\mathcal{S})$ ,  $u$  is continuous on  $\mathcal{S}$  by Sobolev embedding theorem [24]. Note also that  $u \circ \mathcal{P}|_K$  is in  $H^2(K)$  whenever  $u \in H^2(\mathcal{S})$  (by Lemma 1), and thus  $u \circ \mathcal{P}|_K$  is also continuous on  $K$ .

Let  $R_h : H^1(\mathcal{S}) \rightarrow \chi$  be the so-called Ritz projection of  $H^1(\mathcal{S})$  onto  $\chi$ , which is defined as the orthogonal projection with respect to the  $L^2(\mathcal{S})$  inner product. For  $u \in H^1(\mathcal{S})$ ,

$$(\nabla_{\mathcal{S}} R_h u, \nabla_{\mathcal{S}} \omega_h) = (\nabla_{\mathcal{S}} u, \nabla_{\mathcal{S}} \omega_h), \quad \forall \omega_h \in \chi. \quad (30)$$

The following estimates for the Ritz projection are a consequence of Theorem 1.

**Theorem 2.** Let  $u \in H^2(\mathcal{S})$  and  $R_h u \in \chi$  be the Ritz projection defined in (30), then

$$\|R_h u - u\|_{L^2(\mathcal{S})} \leq ch^2 \|u\|_{H^2(\mathcal{S})} \quad (31)$$

and

$$\|\nabla_{\mathcal{S}} (R_h u - u)\|_{L^2(\mathcal{S})} \leq ch \|u\|_{H^2(\mathcal{S})}. \quad (32)$$

We show that the nonlinear reaction terms  $f(u, v) = a - u + u^2 v$  and  $g(u, v) = b - u^2 v$  are Lipschitz continuous, by introducing the concept of *invariant sets* for ordinary differential equations (ODEs) [31]. Consider the following system of ODEs

$$\begin{cases} \partial_t u = \gamma(a - u + u^2 v), \\ \partial_t v = \gamma(b - u^2 v). \end{cases} \quad (33)$$

Let  $\mathcal{I} \subset \mathbb{R}^2$  be a convex region with boundary  $\partial\mathcal{I}$  and let  $\mathbf{n}$  be the unit outward pointing normal vector at  $(u, v) \in \partial\mathcal{I}$  (see Fig. 5). The region  $\mathcal{I}$  is invariant if for any initial conditions in  $\mathcal{I}$  solutions of (33) remain in  $\mathcal{I}$ , that is, if  $(u, v) \in \mathcal{I}$  for all  $t > 0$ . The region  $\mathcal{I}$  is an invariant region if  $\mathbf{n} \cdot (a - u + u^2 v, b - u^2 v) < 0$ , that is if no solution of (33) which reaches  $\partial\mathcal{I}$  leaves  $\mathcal{I}$ , see [6,41].

**Lemma 2.** Let  $\mathcal{I}$  be a convex region in  $\mathbb{R}^2$  whose boundary  $\partial\mathcal{I}$  is given by the quadrilateral ABCDA shown in Fig. 5, where  $A = (u_1, 0)$ , with  $0 < u_1 < a$ , and  $B = (a + b + v_1, 0)$ ,  $C = (a + b, v_1)$  with  $v_1 > \frac{b}{u_1^2}$  and  $D = (u_1, v_1)$ , then  $\mathcal{I}$  is an invariant region of the system (33) which includes the steady state  $(a + b, \frac{b}{(a+b)^2})$ .

**Proof.** The boundary  $\partial\mathcal{I}$  of the convex region  $\mathcal{I}$  consists of line segments AB, BC, CD, and DA. On AB the outward normal  $\mathbf{n} = (0, -1)$ ,  $u_1 \leq u < a + b + v_1$ , and  $v = 0$ , then  $(0, -1) \cdot (a - u + u^2 v, b - u^2 v) = -b + u^2 v = -b < 0$ , since  $b > 0$ . On BC the outward normal  $\mathbf{n} = (1, 1)$ ,  $a + b \leq u \leq a + b + v_1$ , and  $0 \leq v \leq v_1$ , then  $(1, 1) \cdot (a - u + u^2 v, b - u^2 v) = a + b - u < 0$ , since  $u > a + b$ . On CD the outward normal  $\mathbf{n} = (0, 1)$ ,  $u_1 \leq u \leq a + b$ , and  $v = v_1$ , then  $(0, 1) \cdot (a - u + u^2 v, b - u^2 v) = b - u^2 v_1 < 0$ , since  $v_1 > \frac{b}{u_1^2}$ . On DA the outward normal  $\mathbf{n} = (-1, 0)$ ,  $u = u_1$ , and  $0 \leq v \leq v_1$ , then  $(-1, 0) \cdot (a - u + u^2 v, b - u^2 v) = -a + u_1 - u_1^2 v < 0$ , since  $u_1 < a$ .  $\square$

Thus if the initial condition  $(u(0), v(0))$  of the system (33) is in the convex region  $\mathcal{I}$ , then the solution remains in  $\mathcal{I}$  for all  $t > 0$ . We now turn our attention to the model equation (1) and prove that the convex region  $\mathcal{I}$  of Lemma 2 is also an invariant region for (1). The following theorem can be found in [9].

**Theorem 3.** Suppose  $\mathcal{I}$  is a closed convex region with Lipschitz boundary  $\partial\mathcal{I}$  and  $\mathbf{n} \cdot (a - u + u^2 v, b - u^2 v) < 0$ , where  $\mathbf{n}$  is the outward normal to  $\partial\mathcal{I}$ . If  $(u, v)$  satisfies (1) with  $(u_0, v_0) \in \mathcal{I}$ , then  $(u, v) \in \mathcal{I}$  for all  $t > 0$ .

Since the solution  $(u, v)$  of (1) remains in the invariant set  $\mathcal{I}$  provided that initial conditions  $(u_0, v_0) \in \mathcal{I}$ , there exists a number  $\lambda$  such that

$$|u| < \lambda, \text{ and } |v| < \lambda.$$

We now show that the nonlinear reaction terms  $f(u, v) = a - u + u^2 v$  and  $g(u, v) = b - u^2 v$  are locally Lipschitz.

**Lemma 3.** Let  $(u_1, v_1)$  and  $(u_2, v_2)$  be solutions of (1) for initial conditions  $(u_{1,0}, v_{1,0}) \in \mathcal{I}$ , and  $(u_{2,0}, v_{2,0}) \in \mathcal{I}$  respectively, then

$$|f(u_1, v_1) - f(u_2, v_2)| \leq c_1|u_1 - u_2| + c_2|v_1 - v_2|$$

and

$$|g(u_1, v_1) - g(u_2, v_2)| \leq c_3|u_1 - u_2| + c_4|v_1 - v_2|.$$

**Proof.** Since  $(u_1, v_1)$  and  $(u_2, v_2)$  are solutions of (1) and remain in the invariant set  $\mathcal{I}$ , we have  $|u_i| < \lambda$ , and  $|v_i| < \lambda$ ,  $i = 1, 2$ . It follows then that

$$\begin{aligned} |f(u_1, v_1) - f(u_2, v_2)| &= |a - u_1 - u_1^2 v_1 - (a - u_2 - u_2^2 v_2)| \\ &= |u_2 - u_1 + u_2^2 v_2 - u_1^2 v_1| \\ &\leq |u_2 - u_1| + |u_2^2 v_2 - u_1^2 v_2 + u_1^2 v_2 - u_1^2 v_1| \\ &= |u_2 - u_1| + |(u_2^2 - u_1^2)v_2 + u_1^2(v_2 - v_1)| \\ &= |u_2 - u_1| + |(u_2 - u_1)(u_2 + u_1)v_2 + u_1^2(v_2 - v_1)| \\ &\leq (1 + 2\lambda^2)|u_1 - u_2| + \lambda^2|v_2 - v_1|. \end{aligned}$$

Similar analysis yields

$$|g(u_1, v_1) - g(u_2, v_2)| \leq 2\lambda^2|u_1 - u_2| + \lambda^2|v_1 - v_2|. \quad \square$$

Next we derive estimates for the convergence rates of the semi-discrete weak formulation (9). In the following theorem, we suppose that the solutions of the continuous problem are sufficiently smooth, and that they have the regularity implicitly assumed by the presence of the norms on the right hand side of the following inequality.

**Theorem 4.** Let  $(u, v)$  be the solution of (1) and let  $(u_h, v_h) \in X$  be the solution of (9), then

$$\begin{aligned} \|u(t) - u_h(t)\|_{L^2(\mathcal{S})} + \|v(t) - v_h(t)\|_{L^2(\mathcal{S})} &\leq C\|u(0) - u_h(0)\|_{L^2(\mathcal{S})} + \|v(0) - v_h(0)\|_{L^2(\mathcal{S})} \\ &+ ch^2(\|u\|_{H^2(\mathcal{S})} + \|v\|_{H^2(\mathcal{S})}) + \int_0^t ch^2(\|u\|_{H^2(\mathcal{S})} + \|v\|_{H^2(\mathcal{S})} + \|\partial_t u\|_{H^2(\mathcal{S})} + \|\partial_t v\|_{H^2(\mathcal{S})}). \end{aligned}$$

**Proof.** The proof follows the steps as in [51].  $\square$

### 3.3.4. Preservation of the invariant region

Next, we show that the Galerkin approximation constructed using the projection operator can be modified to have the property that  $\mathcal{I}_1$  (a subset of  $\mathcal{I}$ ) is also an invariant region for the approximate solutions. We prove only for the case of a unit sphere. This invariance property is not true in general for the finite element method. The standard Galerkin finite element method does not satisfy the maximum principle. We can however modify the method so that it satisfies a maximum principle by using a lumped mass quadrature rule to approximate the  $L^2$ -inner product in  $\chi$  [51]. Let  $\{\hat{\eta}_i\}_{i=1}^3$  be the vertices of the planar triangle  $K$ , then the lumped mass quadrature rule  $q_K(\hat{u})$  is defined as follows  $q_K = \frac{1}{3}\text{area}(K)\sum_{i=1}^3 \hat{u}(\hat{\eta}_i) \approx \int_K \hat{u}$ .

Using a lumped mass quadrature formula, the mass matrix becomes a diagonal matrix, with the diagonal entry in each row equal to the sum of the entries in the corresponding row of the standard mass matrix  $\tilde{M}$ .

**Proposition 3.** *Let  $K_h$  be a triangulation of the surface of the box  $B$  in which all angles of the triangles are acute (that is less than  $\pi/2$ ), and let  $\mathcal{T}_h$  be the corresponding triangulation of the unit sphere  $S$  constructed by projection operator. Thus,  $\mathcal{P}(K_h) = \mathcal{T}_h$ . Then the stiffness matrix  $\tilde{G}$  has the following properties,  $\tilde{G}_{ii} \geq 0$  and  $\tilde{G}_{ij} \leq 0$ , for  $i \neq j$ . Additionally, let  $I$  be the identity matrix, then the matrix  $(I + \tilde{G})^{-1}$  maps vectors with positive coefficients into vectors with positive coefficients.*

**Proof.** Let us consider a unit sphere. It is clear that the diagonal entries of  $\tilde{G}_{ii}$  are positive, since

$$\tilde{G}_{ii} = (\nabla_S \varphi_i, \nabla_S \varphi_i) = \|\nabla_S \varphi_i\|_{L(S)}^2 \geq 0.$$

We show that  $\tilde{G}_{ij} \leq 0$ , when  $i \neq j$ . Tangential derivatives of the basis functions are the projection of the gradient on to the tangent plane (see (18)). Thus,

$$\nabla_S \varphi_i = P \nabla \varphi_i := \nabla \varphi_i - (\nabla \varphi_i \cdot \mathbf{n}) \mathbf{n}, \quad (34)$$

where

$$P = \begin{bmatrix} 1 - y_1^2 & -y_1 y_2 & -y_1 y_3 \\ -y_1 y_2 & 1 - y_2^2 & -y_2 y_3 \\ -y_1 y_3 & -y_2 y_3 & 1 - y_3^2 \end{bmatrix}$$

and  $\mathbf{n} = (y_1, y_2, y_3)$  is the unit normal to the sphere satisfying  $y_1^2 + y_2^2 + y_3^2 = 1$ . The basis functions  $\varphi_i$  on the unit sphere are constructed by composing the linear basis functions on the cube with the inverse projection  $\mathcal{P}^{-1}$ . The inverse projection from the unit sphere onto the Face 1 of the cube is  $\mathcal{P}_1^{-1} = (1, \frac{y_2}{y_1}, \frac{y_3}{y_1})$ . Here we only consider Face 1, but clearly the same analysis can be repeated for the other faces. From (19) we have  $\nabla \varphi_i = \tilde{J}^T \nabla \hat{\varphi}_i$  where  $\tilde{J}$  is the Jacobian of the inverse projection  $\mathcal{P}_1^{-1}$ . Namely,

$$\tilde{J}^T = \begin{bmatrix} 1 & -\frac{y_2}{y_1^2} & -\frac{y_3}{y_1^2} \\ 0 & \frac{1}{y_1} & 0 \\ 0 & 0 & \frac{1}{y_1} \end{bmatrix}.$$

Combining (34) and (19) we see that  $\nabla_S \varphi_i = P \nabla \varphi_i = P \tilde{J}^T \nabla \hat{\varphi}_i = \tilde{J}^T \nabla \hat{\varphi}_i$  since  $P \tilde{J}^T = \tilde{J}^T$ . Note that,  $\tilde{G}_{ij} = (\nabla_S \varphi_i, \nabla_S \varphi_j) = (\tilde{J}^T \nabla \hat{\varphi}_i, \tilde{J}^T \nabla \hat{\varphi}_j)$ . As shown in [51] the linear basis functions satisfy the inequality,  $(\nabla \hat{\varphi}_i, \nabla \hat{\varphi}_j) \leq 0$ . We now show that the transformation  $\tilde{J}^T$  preserves the angles between vectors. The eigenvalues of  $\tilde{J}^T$  are  $\lambda_1 = 1$ ,  $\lambda_{2,3} = \frac{1}{y_1} = \lambda$ . Clearly  $\tilde{J}^T$  is diagonalizable, having three linearly independent eigenvectors  $u_1, u_2, u_3$ . Consider a triangle formed with the vectors  $u_2, u_3, u_2 - u_3$ . Then the transformation  $\tilde{J}^T$  will transform that triangle to the triangle with edges  $\tilde{J}^T u_2, \tilde{J}^T u_3, \tilde{J}^T(u_2 - u_3)$ . Note that these two triangles are similar since

$$\frac{\|\tilde{J}^T u_2\|_2}{\|u_2\|_2} = \frac{\|\tilde{J}^T u_3\|_2}{\|u_3\|_2} = \frac{\|\tilde{J}^T(u_2 - u_3)\|_2}{\|u_2 - u_3\|_2} = \lambda.$$

Since  $\tilde{J}^T$  preserves the angles between vectors, the result follows.  $\square$

**Remark 5.** Note that we proved Proposition 3 for the projected finite elements on the unit sphere. Computational evidence seem to suggest that it is also true for surfaces such as ellipsoid, cylinders, dumbbells and heart-shaped surfaces, but the proof of such a result involving more complex surfaces remains an open problem.

The proof of the following theorem is inspired by the results in [21].

**Theorem 5.** Let  $\mathcal{I}_1$  be the rectangular region  $[u_1, a+b] \times [0, v_1]$ , that is  $\mathcal{I}_1 \subset \mathcal{I}$ , and let  $L$  denote the maximum of the first partial derivatives, namely  $\frac{\partial f}{\partial u}$  and  $\frac{\partial g}{\partial v}$ . Let  $\mathcal{T}_h$  be the triangulation of the surface  $S$  in which all the angles of the triangles are acute, then if  $\tau \gamma L \leq 1$ , the invariant region  $\mathcal{I}_1$  is invariant for the approximate finite element solution.

**Proof.** Let  $\hat{M}$  denote the lumped mass matrix, and let  $\bar{G}$  denote the stiffness matrix with positive diagonal entries and non-positive off diagonal entries. We consider the following method in the matrix form

$$\begin{cases} \hat{M}\alpha_u^{k+1} + \tau \bar{G}\alpha_u^{k+1} = \hat{M}\alpha_u^k + \tau \gamma f(u_h^{k+1}, v_h^{k+1}), \\ \hat{M}\alpha_v^{k+1} + \tau d\bar{G}\alpha_v^{k+1} = \hat{M}\alpha_v^k + \tau \gamma g(u_h^{k+1}, v_h^{k+1}), \end{cases} \quad (35)$$

where  $f(u_h^{k+1}, v_h^{k+1})$  denotes a vector whose  $j$ th component is  $(a - u_h^{k+1} + (u_h^{k+1})^2 v_h^{k+1}, \varphi_j)$  and similarly  $g(u_h^{k+1}, v_h^{k+1}) = (a - (u_h^{k+1})^2 v_h^{k+1}, \varphi_j)$ .

Let  $u_1$  have the following representation in terms of the finite element basis functions  $u_1 = \sum_{i=1}^n \alpha_{u_{1,i}} \varphi_i(x)$  then  $u_h^k - u_1 = \sum_{i=1}^n (\alpha_u^k - \alpha_{u_{1,i}}) \varphi_i(x)$ . Let  $\alpha$  denote the vector of nodal values, that is  $\alpha = (\alpha_{u_{1,1}}, \alpha_{u_{1,2}}, \dots, \alpha_{u_{1,n}})^T$ . First we assume that  $(u_h^k, v_h^k) \in \mathcal{I}_1$  and show that  $(u_h^{k+1}, v_h^{k+1}) \in \mathcal{I}_1$ . If  $(u_h^k, v_h^k) \in \mathcal{I}_1$ , clearly  $u_h^k - u_1 \geq 0$  and  $v_h^k \geq 0$ , then (35) can be rewritten as

$$\begin{cases} (\hat{M} + \tau \bar{G})(\alpha_u^{k+1} - \alpha) = \hat{M}(\alpha_u^k - \alpha) + \tau \gamma f(u_h^{k+1}, v_h^{k+1}), \\ (\hat{M} + \tau d\bar{G})\alpha_v^{k+1} = \hat{M}\alpha_v^k + \tau \gamma g(u_h^{k+1}, v_h^{k+1}). \end{cases} \quad (36)$$

Thus we want to show that for given non-negative vectors  $\alpha_u^k - \alpha$  and  $\alpha_v^k$ , (36) will produce non-negative vectors. From Taylor's Theorem

$$f(u, v) = f(u_1, 0) + \frac{\partial f}{\partial u}(\xi_1)(u - u_1), \quad \text{for } \xi_1 \in \mathcal{I}_1$$

and

$$g(u, v) = g(u_1, 0) + \frac{\partial g}{\partial v}(\xi_2)v, \quad \text{for } \xi_2 \in \mathcal{I}_1.$$

Then (36) can be rewritten as

$$\left( \hat{M} + \tau \bar{G} - \tau \gamma \frac{\partial f}{\partial u}(\xi_1) \hat{M} \right) (\alpha_u^{k+1} - \alpha) = \hat{M}(\alpha_u^k - \alpha) + \tau \gamma f(u_1, 0)$$

and

$$\left( \hat{M} + \tau d\bar{G} - \tau \gamma \frac{\partial g}{\partial v}(\xi_2) \hat{M} \right) \alpha_v^{k+1} = \hat{M}\alpha_v^k + \tau \gamma g(u_1, 0).$$

The vectors on the right hand side are positive, since  $f(u_1, 0) = a - u_1 > 0$  and  $g(u_1, 0) = b > 0$ . Suppose that the maximum of the first order partial derivatives of  $f$  and  $g$  are denoted by  $L$ , then the left hand side matrix  $\hat{M} + \tau \bar{G} - \tau \gamma \frac{\partial f}{\partial u}(\xi_1) \hat{M}$  has positive diagonal entries and non-negative off diagonal entries provided that  $\tau \gamma L \leq 1$ . Similar analysis can be done for  $a + b - u_h^k \geq 0$  and  $a + b - v_h^k \geq 0$ .  $\square$

**Remark 6.** When computing the solutions of (38) with the method (35) using Picard iteration (and a lumped mass matrix), we obtain identical convergence rates to those shown in Table 1 (for the standard mass matrix), as such these results are not shown.

## 4. Numerical experiments

### 4.1. Parallel computing: Experiment 1

All experiments were performed using Matlab and its Parallel Computing Toolbox. The Picard iteration (15) is carried out, adaptively, several times at each time level. Note that the size of the matrix  $(M + DG + M_u)^{-1}$  increases as the mesh is refined. The finite element method is computationally very intensive. However several steps of the method can be

**Table 1**

Observed errors corresponding to system (38). Here  $j$  denotes the refinement level,  $h$  denotes the diameter of the largest spherical triangle measured using the geodesic distance formula (39),  $n$  denotes the number of spherical triangles.

$j$	$n$	$h$	$\ u - u_h\ $	rate	$\ v - v_h\ $	rate
1	48	0.9553	0.1657		0.1871	
2	192	0.6155	0.0378	3.36	0.0493	3.03
3	768	0.3398	0.0089	2.43	0.0127	2.28
4	3072	0.1750	0.0022	2.11	0.0032	2.08
5	12 288	0.0882	5.5405e-4	2.01	8.1854e-4	1.99
6	49 152	0.0441	1.3854e-4	2.00	2.0513e-4	2.00
7	196 608	0.0221	3.4634e-5		5.1315e-5	

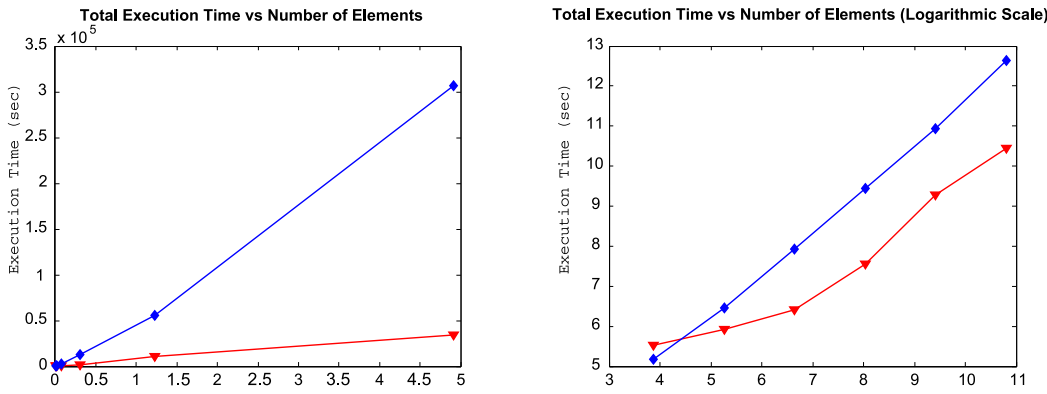


**Fig. 6.** Speedup from parallel computing. Blue (rhombus) line indicates the serial code and the red (triangular arrows) line indicates the parallel code. (a) The figure on the left shows the execution time vs. number of elements for the serial (blue) and the parallel (red) code. (b) The figure on the right shows the execution time using a logarithmic scale for the serial (blue) and the parallel (red) code. (Color version online.)

easily parallelized. Assembling the vectors  $f^l$ , and  $g^l$  which are assembled at every Picard iteration at each time level are the most time consuming operations. Other time consuming operations are the assembly of the mass matrix  $\bar{M}$  and the stiffness matrix  $\bar{G}$  but these are computed only once. We use a parallel *for loop* ("parfor"; part of the parallel computing toolbox) to assemble the matrices  $\bar{M}$ ,  $\bar{G}$ , and vectors  $f^l$  and  $g^l$ .

To demonstrate the performance achieved by performing parallel computations, we execute the parallel and the serial code on several grids with varying numbers of unknowns. The coarse mesh has 48 spherical triangles with mesh size  $h = 0.9553$  and the refined mesh has 196 608 spherical triangles with mesh size  $h = 0.0221$ . The parameters  $\gamma, a, b$ , and  $d$  are held fixed, only the mesh size is reduced by a factor of 1/2 at each refinement step.

For parallel computations we use a computer with the following configuration: Mac Pro with two 2.4 GHz Quad-Core Intel Xeon "Westmere" processors, the computer has 8 cores, thus the parallel code is run using 8 Matlab workers. For comparison, we ran the serial code and plotted the execution times for the various grids in Fig. 6.

#### 4.2. Convergence rates: Experiment 2

In this experiment we verify the convergence rates proved in Theorem 4. We show that an approximate solution obtained by the method described in this paper converges to an "exact" solution as  $h \rightarrow 0$ . We construct an "exact" solution in the following way. Let  $(u, v) = (x_1, x_2)$  be the exact solution of the following elliptic system

$$\begin{cases} -\Delta_S u - \gamma(a - u + u^2 v) = g_1(u, v), \\ -d\Delta_S v - \gamma(b - u^2 v) = g_2(u, v). \end{cases} \quad (37)$$

By prescribing  $g_1(x_1, x_2) = 2x_1 - \gamma(a - x_1 + x_1^2 x_2)$  and  $g_2(x_1, x_2) = 2dx_2 - \gamma(b - x_1^2 x_2)$  it follows that  $(u, v) = (x_1, x_2)$  is the exact solution of (37). Let  $S$  denote the unit sphere, and let  $(u_h, v_h) \in X$  be the approximate solution of the following reaction-diffusion system

**Table 2**

Parameter values used for different illustrative experiments. For details see text.

Expt.	$a$	$b$	$d$	$\gamma$	$\tau$	$n$
1	0.1	0.9	10	60	0.005	–
2	0.1	0.9	10	60	0.005	–
3	0.1	0.9	10	60	0.005	–
4	0.1	0.9	10	500	0.005	12 288
5	0.1	0.9	10	500	0.0025	20 488
6	0.1	0.9	10	500	0.005	8196
7	0.1	0.9	10	–	–	–

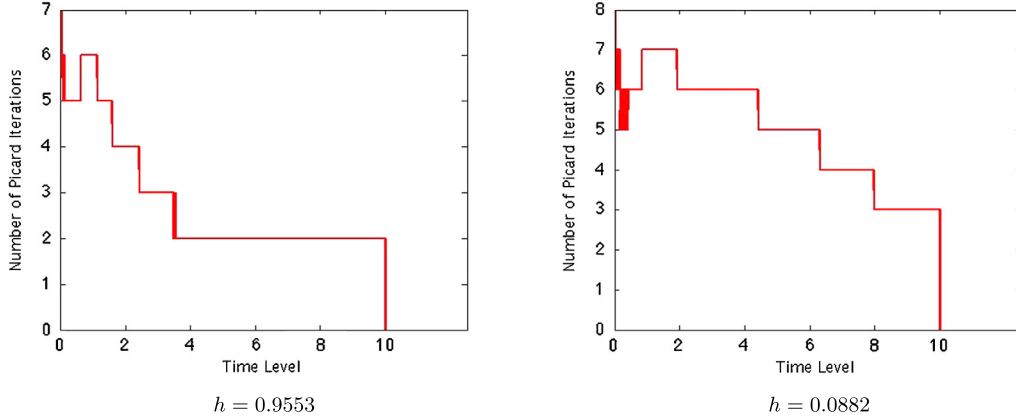


**Fig. 7.** The number of Picard iterations required to reach the stopping criteria at each time level. (Color version online.)

$$\begin{cases} u_t - \Delta_S u = \gamma(a - u + u^2 v) + g_1(x_1, x_2), \\ v_t - d\Delta_S v = \gamma(b - u^2 v) + g_2(x_1, x_2). \end{cases} \quad (38)$$

In [Table 1](#) we see that the approximate solution  $(u_h, v_h) \in X$  converges to the exact solution  $(u, v) = (x_1, x_2)$  as  $h \rightarrow 0$ . For this experiment  $\gamma = 60$ ,  $a = 0.1$ ,  $b = 0.9$  [35], the final time  $T_m = 10$ , and the time step  $\tau = 0.005$  which results in 2000 time steps. The error between the exact solution  $(u, v)$  and the approximate solution  $(u_h, v_h)$  is computed at the final time  $T_m = 10$ , thus

$$\|u - u_h\| = \|u(x, T_m) - u_h(x, T_m)\|_{L^2(S)} \quad \text{and} \quad \|v - v_h\| = \|v(x, T_m) - v_h(x, T_m)\|_{L^2(S)}.$$

Since the triangulation on the sphere is exact and consists of spherical triangles, we use geodesic distance to measure the mesh size  $h$ . The geodesic distance between two points  $x_1$  and  $x_2$  on the unit sphere is the arc length of the great circle connecting them

$$d(x_1, x_2) = \cos^{-1}(x_1 \cdot x_2). \quad (39)$$

#### 4.3. Picard iteration: Experiment 3

To approximate the solution at time level  $k+1$ , we apply the Picard iteration [\(15\)](#). For all the computations presented in this paper, the iteration is stopped (at iteration number  $N_k$ ) when the following convergence criterion are satisfied

$$\|\bar{u}^{l+1}(x, t_{k+1}) - \bar{u}^l(x, t_{k+1})\|_{L^2(S)} \leq 10^{-4} \quad \text{and} \quad \|\bar{v}^{l+1}(x, t_{k+1}) - \bar{v}^l(x, t_{k+1})\|_{L^2(S)} \leq 10^{-4},$$

where  $l = 0, 1, \dots, N_k$ . The above constitutes an adaptive Picard iteration in that  $N_k$  is determined by the above stopping criteria. Parameter values used are given in [Table 2](#). This experiment is carried out on a coarse and on a fine mesh. For the coarse mesh, we take  $h = 0.9553$  with 48 spherical triangles, and for the fine mesh we take  $h = 0.0882$  with 12 288 spherical triangles. The time level versus the number of Picard iterations required to reach the stopping criteria is plotted in [Fig. 7](#). As the time level increases the number of Picard iterations decrease. This is what we expect since the approximate solutions are converging closer and closer to the (steady) exact solution as time increases; requiring less and less Picard iterates in order to satisfy the stopping criteria.

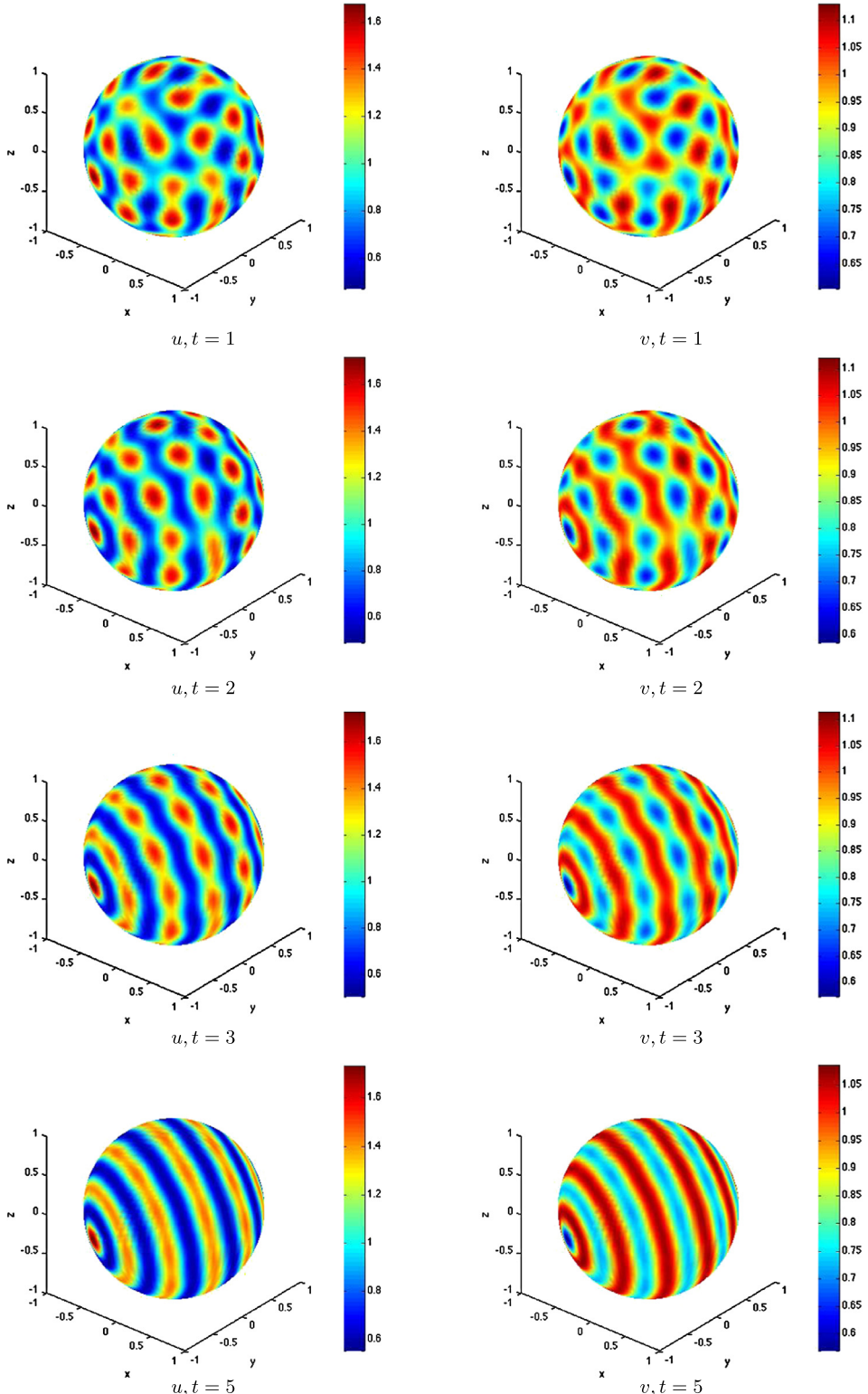


**Fig. 8.** Patterns arising from the reaction-diffusion system (1) on a stationary sphere correspond to the  $u$  and  $v$  chemical concentrations. Parameter values are given in Table 2 (Experiment 4). Spot patterns emerge initially which further evolve into stripe patterns as time increases. We observe a uniform distribution of spot or stripe patterns. The sphere has uniform curvature. (Color version online.)

#### 4.4. The effect of geometry on pattern formation on spheroidal surfaces

##### 4.4.1. Sphere: Experiment 4

In this example we use PFEM to approximate the solution of (1). It must be noted that in the case of a sphere, the PFEM reduces to the radially projected finite element method with the mapping equivalent to the identity. We take  $\mathcal{S}$  to be the unit sphere and use the parameter values given in Table 2 corresponding to *Experiment 4* where  $n$  is the number of spherical triangles in the discretization and  $h$  is the diameter of the largest triangle measured using the geodesic distance formula (39). Initial conditions prescribed are random perturbations around the uniform steady state. This choice of parameters for  $a, b$  and  $\gamma$  is known to satisfy the necessary conditions for diffusion driven instability on fixed domains [35]. The necessary conditions for Turing instability are derived by linear stability analysis and are given in [41]. Turing instability occurs when a uniform steady state which is linearly stable in the absence of diffusion, goes unstable when diffusion is added to the system. These conditions are necessary but not sufficient. For instance, one of the necessary conditions is that the chemicals diffuse at different rates. We impose further restrictions and make one of the chemicals diffuse at a much faster rate than the other. Fig. 8 shows the chemical concentration profiles corresponding to  $u$  and  $v$  as time increases. Notice that the concentration of chemicals  $u$  and  $v$  are “mirror” images of each other; regions with high concentration of chemical  $u$  correspond to regions with low concentration of the chemical  $v$ . Thus rather than showing both of the chemical concentrations, hereafter we only show the chemical concentrations of the chemical  $u$ . We observe the formation of spot patterns emerging from the random perturbations; these in turn evolve to form stripes as time increases. During the evolution process the spatial pattern converges to a spatially inhomogeneous steady state formed of stripes. It can be observed that since the sphere has uniform curvature, patterns are uniformly distributed.

##### 4.4.2. Cylinder: Experiment 5

Next we consider surface  $\mathcal{S}$ , a cylinder with spherical caps defined by

$$1 = \begin{cases} x^2 + y^2 + (z - 1)^2 & \text{if } 1 < z \leq 2, \\ x^2 + y^2 & \text{if } -1 \leq z \leq 1, \\ x^2 + y^2 + (z + 1)^2 & \text{if } -2 < z \leq -1. \end{cases}$$

The radial projection  $P_{\mathcal{R}}$  from the surface of the rectangular box  $B$  onto cylinder  $\mathcal{S}$  is given in (5).

The cylinder has non-uniform curvature and therefore patterns obtained are not uniformly distributed as is the case for the sphere (see Fig. 9).

##### 4.4.3. Ellipsoid: Experiment 6

Next consider the ellipsoidal surface  $\mathcal{S}$  whose equation is given by  $x_1^2 + x_2^2/4 + x_3^2/4 = 1$ . The projection operator  $P$  for this ellipsoidal surface is  $P : B \rightarrow \mathcal{S}$ ,  $P(x) = \frac{\Gamma \|x\|_\infty}{b \|x\|_2} (x_1, 2x_2, 2x_3)$ . The model and numerical parameter values are given in Table 2 *Experiment 6*. Fig. 10 exhibits pattern formation on an ellipsoidal surface. We observe a combination of circular stripes and spots evolving over time to converge to spot patterns. Again surface geometry seems to play a crucial role in the patterns formed. Here, the non-uniform distribution of spot patterns is more pronounced due to the form of the surface geometry. It is clear that non-uniform patterns form depending on the curvature. Therefore we conjecture that geometrical complexities (as those observed in nature) play a crucial role in the formation of patterns (see Fig. 11 for some examples).

##### 4.4.4. The effect of varying $\gamma$ on pattern formation: Experiment 7

Next we explore the effects of varying the parameter  $\gamma$  on patterns formed on arbitrary spheroidal surfaces (see Fig. 11). We vary  $\gamma$  ( $\gamma = 10, 29, 60, 200$ ) and keep all other parameter values fixed as in Table 2 [35]. The rationale is to demonstrate the role of surface geometry on pattern formation. On planar stationary domains it can be shown that  $\gamma$  is proportional to the square of the length scale of the domain [41]. For example, doubling the value of  $\gamma$  implies doubling the domain size. This translates to an increase in pattern complexity. The same phenomena is observed on surfaces as well. Increasing  $\gamma$  for each particular surface results in more complex patterns being formed (see Fig. 11). However, each surface has different patterns for a fixed value of  $\gamma$ .

**Remark 7.** We note that the spatially inhomogeneous steady states observed for the different surfaces depend crucially on the initial conditions as well as the model parameter values. Depending on the symmetry properties of the surfaces, symmetrical solutions can also be observed (results not shown).

## 5. Conclusion, discussion and future research strands

Modeling, analysis and simulation of reaction-diffusion systems on arbitrary surfaces is a young and emerging research area with numerous applications in developmental biology, cancer research, wound healing, cell motility and bio-medical engineering. In this paper we proposed and used for the first time the projected finite element method (PFEM) to solve complex nonlinear reaction-diffusion systems on stationary surfaces. The development of the numerical methodology gives

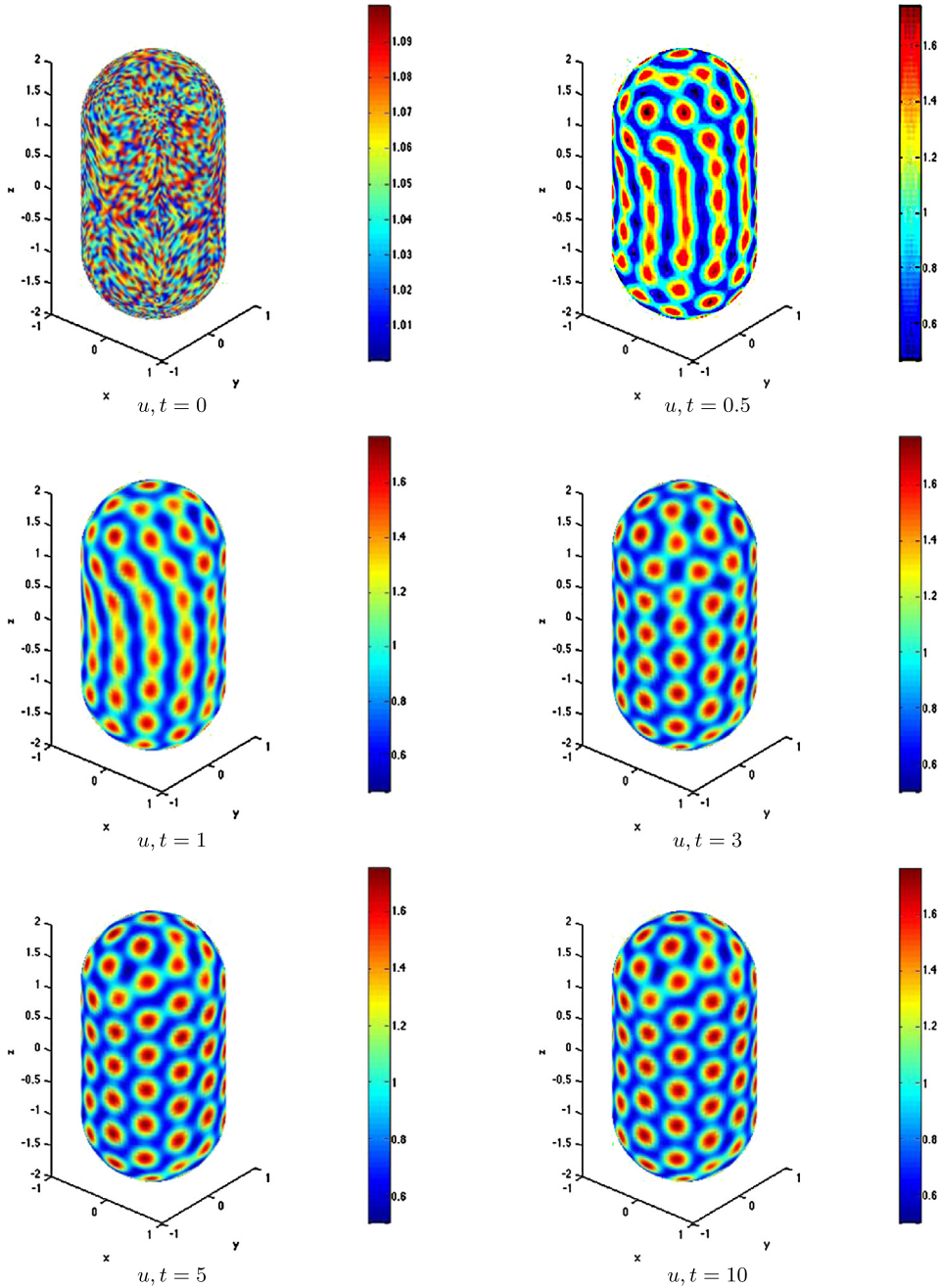


**Fig. 9.** Patterns arising from the reaction-diffusion system (1) on a stationary cylinder correspond to the  $u$  chemical concentration. Stripe patterns emerge which evolve into spot patterns as time increases. Parameter values are given in Table 2 (Experiment 5). Observe how patterns are non-uniformly distributed and seem to depend on the curvature which is non-uniform across the cylinder. (Color version online.)

us a platform to carry out detailed biological and biomedical research where models are posed on surfaces (which could potentially change continuously in time – part of our ongoing research).

It must be noted however that in some practical situations the analytic description of the surface will not be available. For the case when there is no analytic description of the surface, the surface can be approximated, for instance by splines. And then one can construct approximate projection operators. In this case, the PFE method will no longer be confirming. This forms part of our current studies.

In this article we have obtained convergence results for the PFEM and have shown that solutions converge accurately to real physical solutions as the mesh size is refined. In order to speed up computations we have employed parallel computing; it is now possible to obtain solutions in a couple of hours rather than weeks as is the case when using a single processor. We

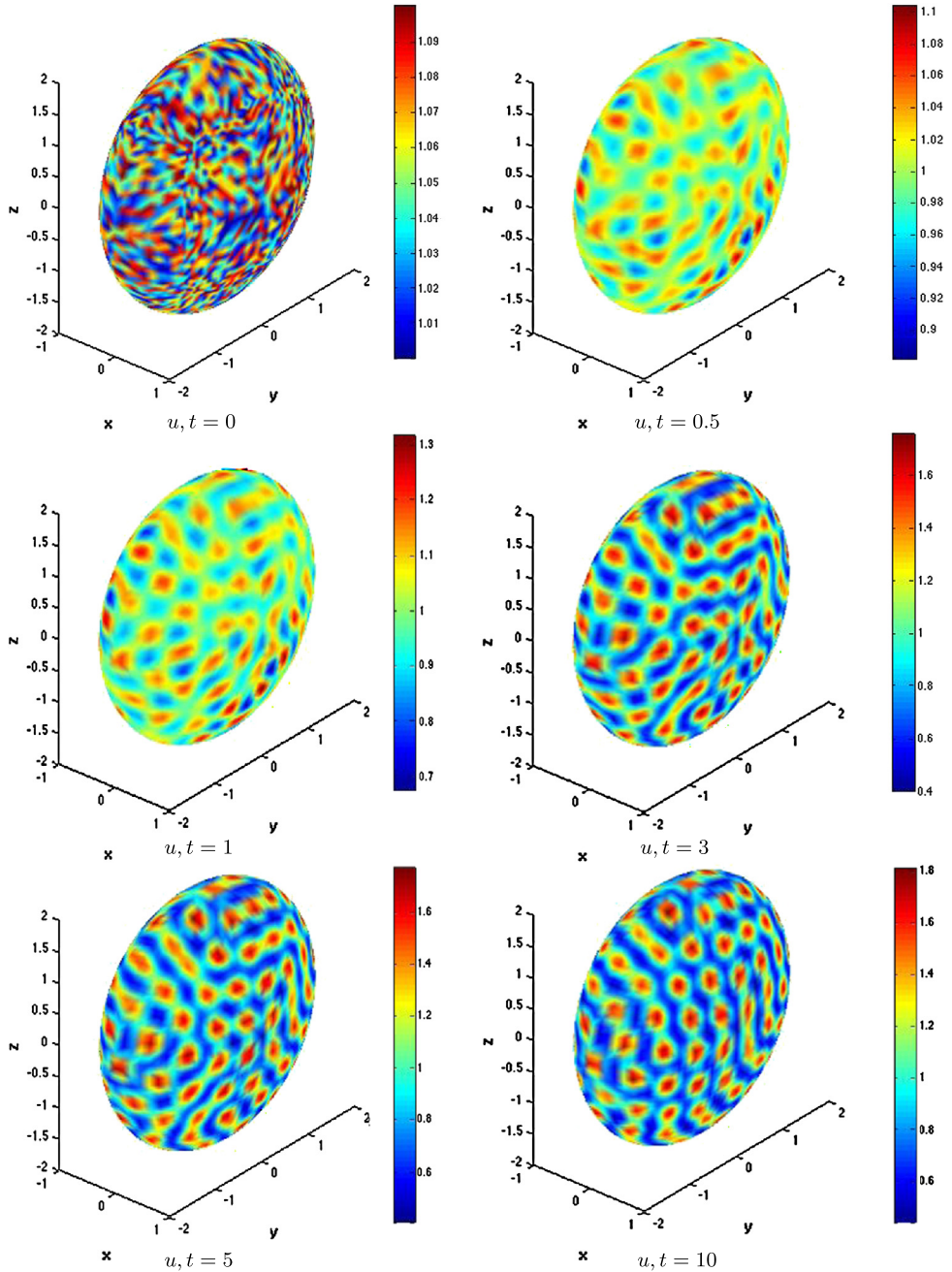
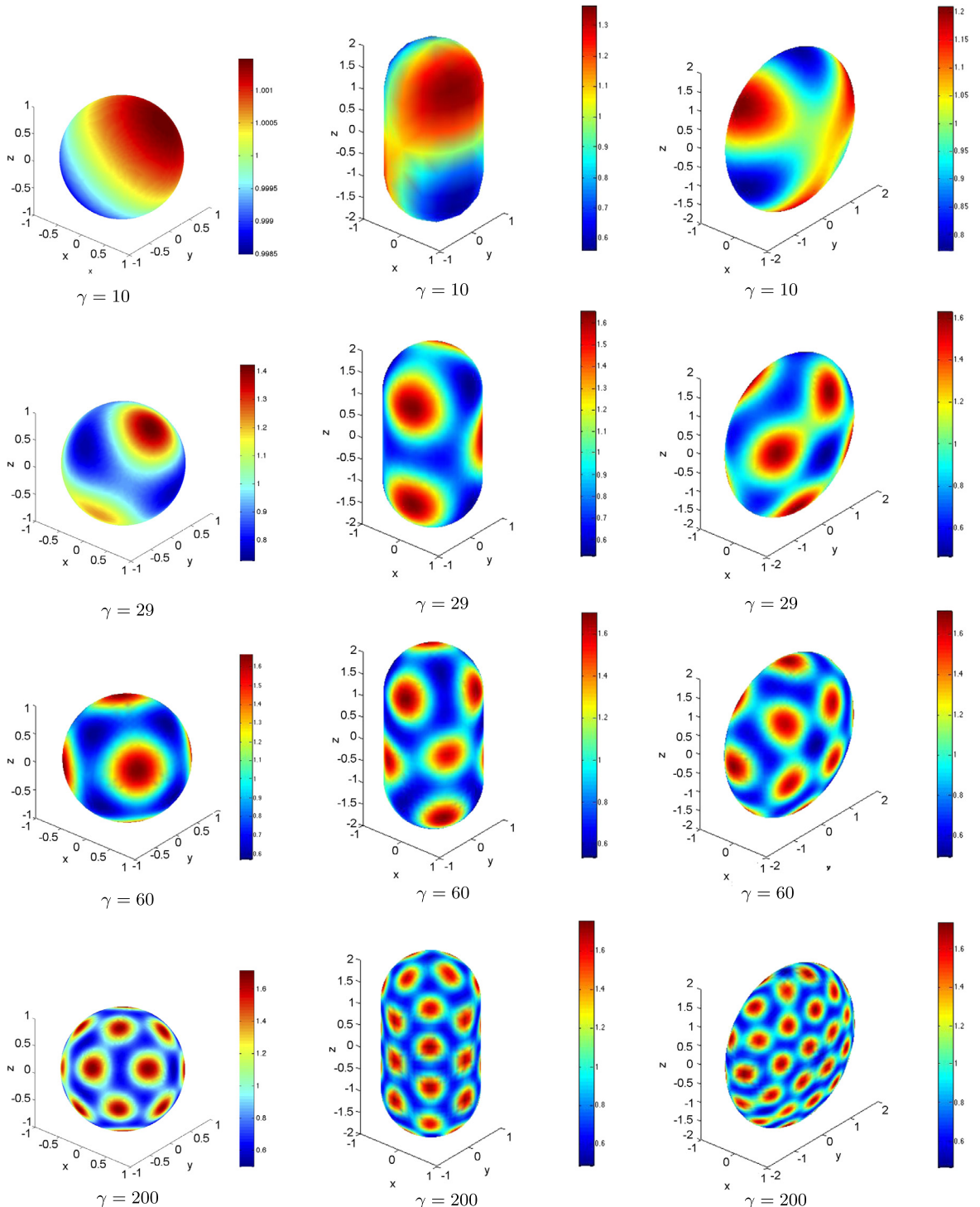


**Fig. 10.** Patterns arising from the reaction-diffusion system (1) on a stationary ellipsoid correspond to the  $u$  chemical concentration. Stripe and spot patterns evolve into spot patterns as time increases. Parameter values are given in Table 2 (Experiment 6). Again, patterns are non-uniformly distributed depending on the curvature. (Color version online.)

treated nonlinear reaction-kinetics differently from the way these were previously handled. We proposed and implemented an adaptive Picard iteration. On stationary surfaces we demonstrated computationally that for a given accuracy only a small number of Picard iterations are needed, and that this number goes down over time, as the solution approaches a steady state. As time increases a single Picard iteration becomes sufficient thereby speeding up computations. At the initial stages of the computations approximately 5 Picard iterations are required for accuracy of  $10^{-4}$ .

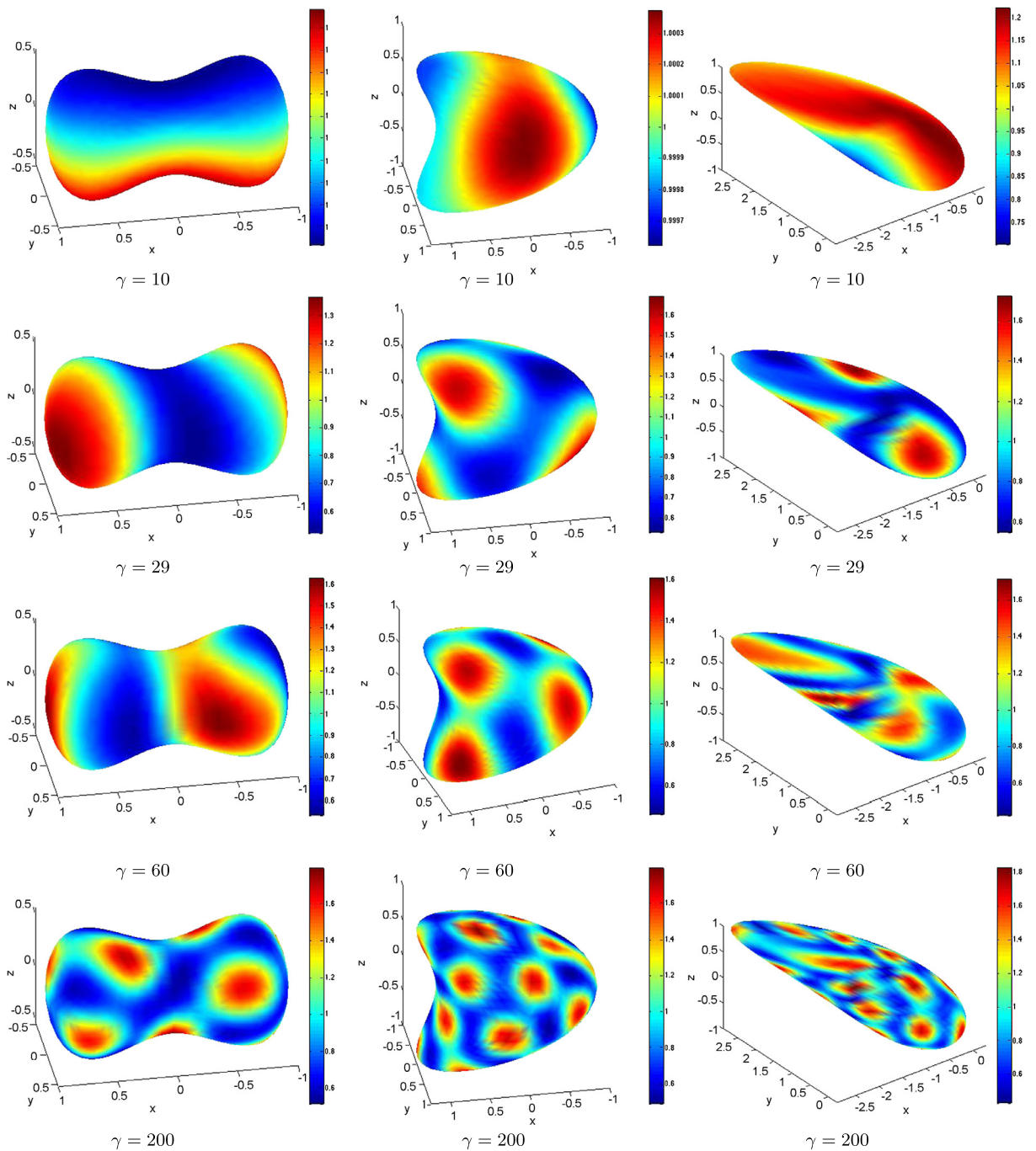
We emphasize that:

- Surface geometry plays a crucial role in pattern formation. Unlike one- or two-dimensional studies where surface geometrical properties cannot be taken into account, solving reaction-diffusion equations on different surfaces for a set



**Fig. 11.** Patterns arising from the reaction–diffusion system (1) on stationary surfaces correspond to the  $u$  chemical concentration for increasing values of  $\gamma$ . The rest of the model parameter values are fixed as in Table 2 (Experiment 7). The results clearly demonstrate the role of surface geometry and the parameter  $\gamma$  to pattern formation. (Color version online.)

of fixed parameter values results in different pattern transitions and convergence to spatially inhomogeneous solutions. This raises theoretical questions about the role of surface geometry (and curvature) on pattern formation and is the subject of our current studies.

**Fig. 11. (continued)**

- As for planar domains, variations in  $\gamma$  result in the emergence of complex patterns which depend on the type of the surface under consideration.
- We have proved that a subset of the invariant region for the solutions of the partial differential system is also an invariant region for the finite element solution.
- The PFEM presented in this paper differs from the other methods in the literature by (i) exact discretization of the spheroidal surfaces and (ii) by constructing a conforming finite element method.

In developmental and biomedicine it is clear that patterns form during growth development [41,26]. This raises a host of questions on modeling, analysis, numerical analysis, and simulations of partial differential equations (of which reaction-

diffusion systems are an example) on arbitrary evolving surfaces. In this article we have set the foundation to tackle the following problems:

- Extend the PFEM to approximate solutions of complex systems of partial differential equations on continuously evolving spheroidal surfaces.
- Carry out detailed numerical analysis (a priori and a posteriori error estimates) of systems of partial differential equations where surface evolution is unknown and is modeled from biological, biochemical, or bio-mechanical experiments.
- Ultimately we would like to study the role of surface geometry from theoretical and computational points of view. Results in this article clearly demonstrate that surface geometry plays a key role in pattern formation. Preliminary studies by Venkataraman et al., [54] on parr mark pattern formation in the Amago Trout show that curvature could play a pivotal role in determining the pattern selection mechanism during growth development.
- Finally, the generality, applicability, accuracy and efficiency of the projected finite element method makes it possible to tackle biological and biomedical application where surface evolution and geometry are crucial properties.

## Acknowledgements

The research of Necibe Tuncer has been partially supported by the NSF under grant DMS-1220342.

This work (AM) is supported by the following grants: EPSRC research grant (EP/J016780/1): *Modeling, analysis and simulation of spatial patterning on evolving surfaces*, The Leverhulme Trust Research Project Grant (RPG-2014-149): *Unravelling new models for 3D cell migration* and the British Council through its UK-US New Partnership Fund (PMI2): *Strengthening the UK, US and Southern African human infrastructure in Mathematical Sciences*.

The research of AJM has been partially supported by the NSF under grant DMS-0915045. This material (AJM) is based upon work supported by (while serving at) the National Science Foundation. Any opinion, findings, and conclusions or recommendations expressed in this material are those of the author(s) and do not necessarily reflect the views of the National Science Foundation.

## References

- [1] R. Barreira, C.M. Elliott, A. Madzvamuse, The surface finite element method for pattern formation on evolving biological surfaces, *J. Math. Biol.* 63 (6) (2011) 1095–1119.
- [2] R. Barrio, R. Baker, B. Vaughan Jr, K. Tribuzi, M. de Carvalho, R. Bassanezi, P. Maini, Modeling the skin pattern of fishes, *Phys. Rev. E* 79 (3) (2009), 031908–11.
- [3] D. Braess, *Finite Elements. Theory, Fast Solvers, and Applications in Elasticity Theory*, third edition, Cambridge University Press, Cambridge, 2007.
- [4] S.C. Brenner, L.R. Scott, *The Mathematical Theory of Finite Element Methods*, second edition, Texts in Applied Mathematics, vol. 15, Springer-Verlag, New York, 2002.
- [5] G. Caginalp, Stefan and Hele-Shaw type models as asymptotic limits of the phase-field equations, *Phys. Rev. A* 39 (11) (1989) 5887–5896.
- [6] R.S. Cantrell, C. Cosner, *Spatial Ecology Via Reaction-Diffusion Equations*, Wiley Series in Mathematical and Computational Biology, John Wiley & Sons Ltd., Chichester, 2003.
- [7] M.A.J. Chaplain, M. Ganesh, I.G. Graham, Spatio-temporal pattern formation on spherical surfaces: numerical simulation and application to solid tumour growth, *J. Math. Biol.* 42 (5) (2001) 387–423.
- [8] P.G. Ciarlet, *The Finite Element Method for Elliptic Problems*, Classics in Applied Mathematics, vol. 40, Society for Industrial and Applied Mathematics (SIAM), Philadelphia, PA, 2002.
- [9] C. Cosner, Unpublished Lecture Notes, 2006.
- [10] K. Deckelnick, G. Dziuk, C.M. Elliott, Computation of geometric partial differential equations and mean curvature flow, *Acta Numer.* 14 (2005) 139–232.
- [11] R. Dillon, P.K. Maini, H.G. Othmer, Pattern formation in generalized Turing systems. I. Steady-state patterns in systems with mixed boundary conditions, *J. Math. Biol.* 32 (4) (1994) 345–393.
- [12] M. Do Carmo, *Differential Geometry of Curves and Surfaces*, Prentice-Hall, New Jersey, 1976.
- [13] A. Donna, C. Helzel, A finite volume method for solving parabolic equations on logically Cartesian curved surface meshes, *SIAM J. Sci. Comput.* 31 (6) (2009) 4066–4099.
- [14] D.A. Dunavant, High degree efficient symmetrical Gaussian quadrature rules for the triangle, *Int. J. Numer. Methods Eng.* 21 (6) (1985) 1129–1148.
- [15] G. Dziuk, C.M. Elliott, Finite elements on evolving surfaces, *IMA J. Numer. Anal.* 27 (2) (2007) 262–292.
- [16] G. Dziuk, C.M. Elliott, Surface finite elements for parabolic equations, *J. Comput. Math.* 25 (4) (2007) 385–407.
- [17] G. Dziuk, C.M. Elliott, Eulerian finite element method for parabolic PDEs on implicit surfaces, *Interfaces Free Bound.* 10 (1) (2008) 119–138.
- [18] G. Dziuk, C.M. Elliott, An Eulerian approach to transport and diffusion on evolving implicit surfaces, *Comput. Vis. Sci.* 13 (1) (2010) 17–28.
- [19] G. Dziuk, C.M. Elliott, Finite element methods for surface PDEs, *Acta Numer.* 22 (2013) 289–396.
- [20] C.M. Elliott, B. Stinner, R. Styles, R. Welford, Numerical computation of advection and diffusion on evolving diffuse interfaces, *IMA J. Numer. Anal.* 31 (3) (2011) 786–812.
- [21] D.J. Estep, M.G. Larson, R.D. Williams, Estimating the error of numerical solutions of systems of reaction–diffusion equations, *Mem. Am. Math. Soc.* 146 (696) (2000).
- [22] A. Gierer, H. Meinhardt, Theory of biological pattern formation, *Kybernetik* 12 (1) (1972) 30–39.
- [23] J.B. Greer, A.L. Bertozzi, G. Sapiro, Fourth order partial differential equations on general geometries, *J. Comput. Phys.* 216 (1) (2006) 216–246.
- [24] E. Hebey, *Sobolev Spaces on Riemannian Manifolds*, Springer, Berlin, 2007.
- [25] S.E. Hieber, P. Koumoutsakos, A Lagrangian particle level set method, *J. Comput. Phys.* 210 (1) (2005) 342–367.
- [26] S. Kondo, R. Asai, A reaction–diffusion wave on the skin of the marine angelfish pomacanthus, *Nature* 376 (6543) (1995) 765–768.
- [27] S. Larsson, V. Thomée, *Partial Differential Equations with Numerical Methods*, Texts in Applied Mathematics, vol. 45, Springer-Verlag, Berlin, 2009.
- [28] J.M. Lee, *Riemannian Manifolds*, Graduate Texts in Mathematics, vol. 176, Springer-Verlag, New York, 1997, An introduction to curvature.
- [29] J. Lefèvre, J.-F. Mangin, A reaction–diffusion model of human brain development, *PLoS Comput. Biol.* 6 (4) (2010) e1000749.
- [30] S.S. Liaw, C.C. Yang, R.T. Liu, J.T. Hong, Turing model for the patterns of lady beetles, *Phys. Rev. E* 64 (2001) 041909.

- [31] J.D. Logan, An Introduction to Nonlinear Partial Differential Equations, second edition, Pure and Applied Mathematics, Wiley-Interscience, Hoboken, NJ, 2008.
- [32] C.B. Macdonald, B. Merriman, S.J. Ruuth, Simple computation of reaction-diffusion processes on point clouds, Proc. Natl. Acad. Sci. USA 110 (23) (2013) 9209–9214.
- [33] C.B. Macdonald, S.J. Ruuth, The implicit closest point method for the numerical solution of partial differential equations on surfaces, SIAM J. Sci. Comput. 31 (6) (2009/2010) 4330–4350.
- [34] A. Madzvamuse, A numerical approach to the study of spatial pattern formation, Ph.d. thesis, University of Oxford, 2000.
- [35] A. Madzvamuse, Time-stepping schemes for moving grid finite elements applied to reaction-diffusion systems on fixed and growing domains, J. Comput. Phys. 214 (1) (2006) 239–263.
- [36] A. Madzvamuse, R.D.K. Thomas, P.K. Maini, A.J. Wathen, A numerical approach to the study of spatial pattern formation in the ligaments of arcid bivalves, Bull. Math. Biol. 64 (2002) 501–530.
- [37] A. Madzvamuse, A.J. Wathen, P.K. Maini, A moving grid finite element method applied to a model biological pattern generator, J. Comput. Phys. 190 (2) (2003) 478–500.
- [38] H. Meinhardt, The Algorithmic Beauty of Sea Shells, The Virtual Laboratory, Springer-Verlag, Berlin, 1995.
- [39] A.J. Meir, N. Tuncer, Radially projected finite elements, SIAM J. Sci. Comput. 31 (3) (2009) 2368–2385.
- [40] J.D. Murray, Parameter space for Turing instability in reaction diffusion mechanisms: a comparison of models, J. Theor. Biol. 98 (1) (1982) 143–163.
- [41] J.D. Murray, Mathematical Biology. I An Introduction, third edition, Interdisciplinary Applied Mathematics, vol. 17, Springer-Verlag, New York, 2002.
- [42] S. Osher, R. Fedkiw, Level Set Methods and Dynamic Implicit Surfaces, Applied Mathematical Sciences, vol. 153, Springer-Verlag, New York, 2003.
- [43] K.J. Painter, H.G. Othmer, P.K. Maini, Stripe formation in juvenile Pomacanthus explained by a generalized Turing mechanism with chemotaxis, Proc. Natl. Acad. Sci. 96 (1999) 5549–5554.
- [44] I. Prigogine, R. Lefever, Symmetry breaking instabilities in dissipative systems II, J. Chem. Phys. 48 (1968) 1695–1700.
- [45] S.J. Ruuth, Implicit-explicit methods for reaction-diffusion problems in pattern formation, J. Math. Biol. 34 (2) (1995) 148–176.
- [46] J. Schnakenberg, Simple chemical reaction systems with limit cycle behavior, J. Theor. Biol. 81 (3) (1979) 389–400.
- [47] T. Sekimura, A. Madzvamuse, A. Wathen, P. Maini, A model for colour pattern formation in the butterfly wing of Papilio dardanus, Proc. R. Soc. B, Biol. Sci. 267 (1446) (2000) 851–859.
- [48] J.A. Sethian, Level set methods and fast marching methods, in: Evolving Interfaces in Computational Geometry, Fluid Mechanics, Computer Vision, and Materials Science, second edition, in: Cambridge Monographs on Applied and Computational Mathematics, vol. 3, Cambridge University Press, Cambridge, 1999.
- [49] S. Sick, S. Reinker, J. Timmer, T. Schlaake, WNT and DKK determine hair follicle spacing through a reaction-diffusion mechanism, Science 314 (5804) (2006) 1447–1450.
- [50] D. Thomas, Artificial enzyme membrane, transport, memory and oscillatory phenomena, in: D. Thomas, J.-P. Kervenez (Eds.), Analysis and Control of Immobilised Enzyme Systems, Springer-Verlag, Berlin, 1975, pp. 115–150.
- [51] V. Thomée, Galerkin Finite Element Methods for Parabolic Problems, second edition, Springer Series in Computational Mathematics, vol. 25, Springer-Verlag, Berlin, 2006.
- [52] N. Tuncer, A novel finite element discretization of domains with spheroidal geometry, Ph.D. Dissertation, Auburn University Libraries, 2007.
- [53] A.M. Turing, The chemical basis of morphogenesis, Philos. Trans. R. Soc. Lond. 237 (641) (1952) 37–72.
- [54] C. Venkataraman, T. Sekimura, E.A. Gaffney, P.K. Maini, A. Madzvamuse, A model for parr mark pattern formation during the early development of Amago trout, Phys. Rev. E 84 (2011) 041923.